JOURNAL OF PETROLOGY | VOLUME 55 | NUMBER 4 | PAGES 769–802 | 2014 | doi:10.1093/petrology/egu006

Quaternary Sanukitoid-like Andesites Generated by Intracrustal Processes (Chacana Caldera Complex, Ecuador): Implications for Archean Sanukitoids

MASSIMO CHIARADIA[1]*, OTHMAR MÜNTENER[2] AND BERNARDO BEATE[3]

[1]SECTION OF EARTH AND ENVIRONMENTAL SCIENCES, UNIVERSITY OF GENEVA, RUE DES MARAÎCHERS 13, 1205 GENEVA, SWITZERLAND

[2]INSTITUTE OF EARTH SCIENCES, UNIVERSITY OF LAUSANNE, GÉOPOLIS, 1015 LAUSANNE, SWITZERLAND

[3]DEPARTMENT OF GEOLOGY, ESCUELA POLITECNICA NACIÓNAL, QUITO, ECUADOR

RECEIVED MAY 27, 2013; ACCEPTED JANUARY 21, 2014

High-Mg diorites enriched in incompatible elements and their extrusive equivalents are rare subduction-related rock types that have been found in modern arc settings and in Late Archean sequences, where they are associated with trondhjemite–tonalite–granodiorite (TTG) suites. Archean rocks with these geochemical features are known as sanukitoids and, despite their limited abundance, are considered to be the indicators of the onset of modern plate tectonics because of their similarities to modern subduction-related high-Mg andesites and diorites. Understanding the genesis of sanukitoid rocks is thus an essential step towards understanding crustal growth processes. The accepted petrogenetic models for modern, enriched, high-Mg andesites and their Archean equivalents, the sanukitoids, consist of metasomatic enrichment of the mantle wedge by slab components and its subsequent partial melting, or the modification of siliceous slab components through continuous reaction with mantle peridotite during their ascent through the mantle wedge. We present new data on the petrography, mineral chemistry and whole-rock geochemistry (major and trace elements and Sr–Nd–Pb isotopes) of andesitic rocks from an ~30 ka lava flow (Yuyos flow) from the Chacana Caldera Complex, Eastern Cordillera of Ecuador. These rocks show a remarkable geochemical affinity with Archean sanukitoids, including high magnesium numbers (0·58–0·63) accompanied by high contents of incompatible elements (e.g. Th 17–23 ppm, U 6–7·5 ppm, Ba 1600–1800 ppm, Sr 1430–1565 ppm, La 74–94 ppm). Additionally, the sanukitoid-like andesites of Yuyos are associated with predominant silica-rich (adakite-like) andesites, which are widespread throughout the Quaternary arc of Ecuador. This makes the Quaternary Ecuadorian magmatic province a close equivalent of the Archean TTG–sanukitoid association. The bulk-rock geochemistry, petrography and mineral chemistry data indicate that the sanukitoid-like features of the andesites of the Yuyos flow derive from intracrustal recycling of the felsic–intermediate to mafic–ultramafic roots of the Quaternary volcanic arc of Ecuador by 'normal' mantle-derived basaltic magmas with the geochemical characteristics of continental arc basalts or high-alumina basalts. In view of the similarities between the Yuyos andesites and Archean sanukitoids in terms of geochemistry and lithological association, we suggest that genetic models should consider the possibility of intracrustal recycling as a process responsible for the peculiar signatures of both Archean sanukitoids and modern enriched high-Mg andesites.

KEY WORDS: *Ecuador; andesite; sanukitoid; Archean magmatism*

INTRODUCTION

The origin, composition and secular evolution of the continental crust is a continuing matter of debate. Although it is generally accepted that most continental crust

*Corresponding author. Telephone: +41 22 379 66 34. Fax: +41 22 379 32 10. E-mail: Massimo.Chiaradia@unige.ch.

production today is associated with subduction zones, there is much uncertainty about similar processes acting in the Archean. Statistical geochemistry indicates that mantle potential temperatures, degrees of melting and the nature of felsic derivatives were different in the Archean (Keller & Schoene, 2012), with a predominance of high-Na tonalite–trondjemite–granodiorite (TTG) suites. This changed about 2·5 Gyr ago with the onset of modern-style plate tectonics characterized by subduction zones and associated arc magmatism (Martin & Moyen, 2002; Martin *et al.*, 2010; Keller & Schoene, 2012). It has been proposed (Martin *et al.*, 2010) that this geochemical transition at the Archean–Proterozoic boundary is characterized by the formation of particular rocks, named Archean sanukitoids [high-Mg diorite–tonalite–granodiorite series; Shirey & Hanson 1984; however, see Tatsumi (2006) for the improper use of the term 'sanukitoid' applied to Archean intrusive rocks]. Therefore, the petrogenesis of Archean sanukitoids may have profound implications for the understanding of crustal growth mechanisms and the onset of plate-tectonic processes in the Late Archean (e.g. Tatsumi, 2008; Martin *et al.*, 2010).

The trace element composition of Archean sanukitoids is matched to a good extent (Fig. 1) by that of Cenozoic and Quaternary enriched high-Mg andesites (HMA) such as 'bajaites' (e.g. Calmus *et al.*, 2003) and low-silica adakites (LSA: Martin *et al.*, 2005). Like the Archean sanukitoids, enriched HMA and 'bajaites' (LSA) are relatively rare in Phanerozoic subduction-related settings (e.g. Aleutian islands; Mt. Shasta, California; Miocene Setouchi belt, Japan; Baja California, Mexico: Calmus *et al.*, 2003; Kelemen *et al.*, 2003; Grove *et al.*, 2005; Tatsumi, 2006; Wood & Turner, 2009). On the basis of their geochemical similarities, Archean sanukitoids and their Phanerozoic equivalents are thought to have formed through similar processes. Because of their high Mg# [molar Mg/$(Mg + Fe_{tot})$] and Ni and Cr contents, enriched HMA (LSA) and Archean sanukitoids are considered to have been in equilibrium with mantle peridotite; however, at the same time, the elevated contents of large ion lithophile elements (LILE), light rare earth elements (LREE) and some high field strength elements (HFSE) require some sort of 'crustal' input. The widely accepted 'crustal' input in enriched HMA (LSA) and Archean sanukitoids is a siliceous slab component derived from partial melting of the subducting plate (e.g. Yogodzinski *et al.*, 1994, 1995; Kelemen *et al.*, 2003; Martin *et al.*, 2005; Tatsumi, 2008). This slab component may either metasomatize the mantle wedge prior to subsequent flux- or decompression-melting generating andesitic or dacitic melts (Rapp *et al.*, 1999), or, alternatively, undergo incomplete reaction with the surrounding mantle peridotite and ascend into the crust as a modified residual andesitic or dacitic slab melt (e.g. Yaxley & Green, 1998; Kelemen *et al.*, 2003; Martin *et al.*, 2005). In both cases slab component–peridotite reactions are characterized by consumption of olivine and crystallization of orthopyroxene ± garnet with a consequent decrease of SiO_2 and increase of MgO in the reacted melt (= enriched HMA or LSA) and increase of incompatible elements that cannot be accommodated in the newly crystallizing phases.

In this paper we report and discuss petrographic observations and geochemical data for whole-rocks, minerals, interstitial melts and melt inclusions from a Pleistocene andesitic lava flow from the Chacana Caldera Complex (CCC), Ecuador, hereafter termed the Yuyos andesite. The geochemistry of this lava flow strongly resembles that of Cenozoic–Quaternary enriched HMA (LSA) and has even more affinity with the geochemistry of Archean sanukitoids (Fig. 1). Because the Quaternary arc magmatism of Ecuador is characterized by widespread adakite-like magmatism (broadly comparable with Archean TTG signatures), the Quaternary Ecuadorian association of abundant adakite-like and rare sanukitoid-like magmatism can be viewed as a proxy for the Late Archean association of abundant TTG and rarer sanukitoids. We show that the geochemistry of the Yuyos andesite corresponds to that of sanukitoids and is the result of intracrustal processes, and that slab melting processes, although not excluded in the source region, are not responsible for this geochemistry. We discuss the implications of this conclusion for the genetic interpretation of Archean sanukitoids and crustal growth processes.

GEODYNAMIC SETTING AND ARC MAGMATISM

The geology of the Ecuadorian Andes is characterized by the accretion of terranes of both continental and oceanic affinity (Fig. 2a) from the Late Jurassic to the Late Cretaceous (Feininger, 1987; Jaillard *et al.*, 1990, 1997; Aspden & Litherland, 1992; Litherland *et al.*, 1994; Noble *et al.*, 1997; Kerr *et al.*, 2002; Mamberti *et al.*, 2003; Spikings *et al.*, 2005; Vallejo *et al.*, 2006, 2009). Present-day arc volcanism in the Ecuadorian Andes is the result of subduction of the 12–20 Myr old Nazca plate and aseismic Carnegie Ridge (Fig. 2a). The active to recent volcanic arc of Ecuador extends over more than 100 km across the Andean chain starting in the Western Cordillera, passing through the Interandean Valley and the Eastern Cordillera, and ending in the Andean foreland (Oriente) where both alkaline (Sumaco, Pan de Azucar) and calc-alkaline (Reventador) volcanoes occur. Such a broad volcanic arc contrasts with the narrow volcanic arc immediately to the north, in Colombia, and with the volcanic gap south of 2°S, which is dominated by the Peruvian flat slab segment (Barazangi & Isacks, 1976). The subduction of the aseismic Carnegie Ridge, coincident with the

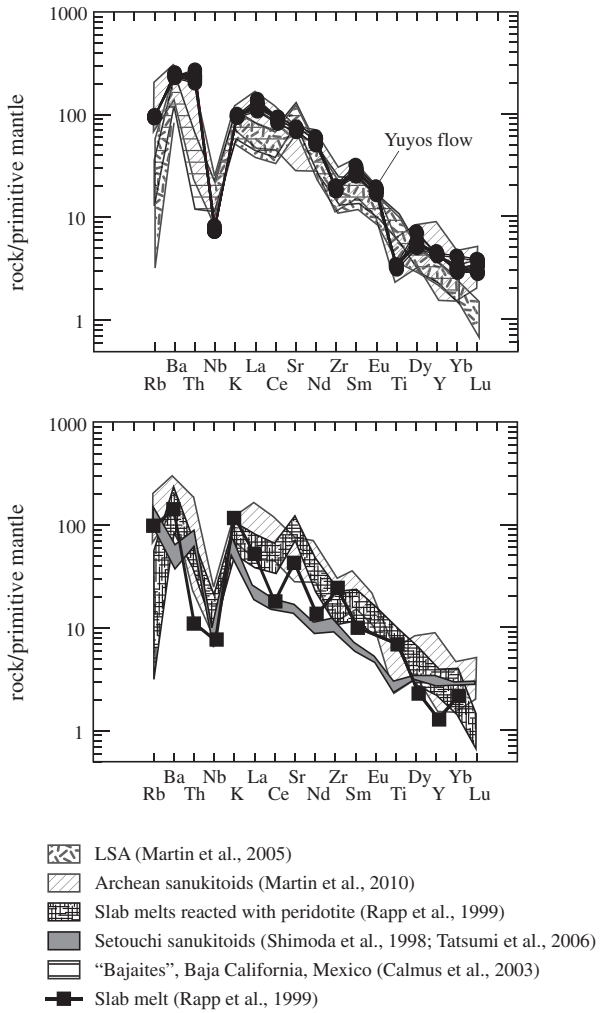

Fig. 1. Primitive mantle-normalized trace element patterns for average Archean sanukitoids ±1σ (Martin *et al.*, 2010), low-silica Quaternary adakites ±1σ (LSA, Martin *et al.*, 2005), eclogitic slab melt and slab melt reacted with peridotites (Rapp *et al.*, 1999), Setouchi sanukitoids (Shimoda *et al.*, 1998; Tatsumi *et al.*, 2006), and 'bajaites' from Baja California, Mexico (Calmus *et al.*, 2003).

Ecuadorian volcanic arc, suggests a direct link with arc broadening. Subduction of the Carnegie Ridge beneath the continental crust of Ecuador has caused an increased coupling between the subducting and overriding plates (Ego *et al.*, 1996; Gutscher *et al.*, 1999; Graindorge *et al.*, 2004; Sage *et al.*, 2006). Gutscher *et al.* (1999) proposed flat subduction coincident with subduction of the Carnegie Ridge flanked by the subduction of two steeper segments to the north and south of the Carnegie Ridge, separated by two tear zones. In contrast, Guillier *et al.* (2001) concluded that subduction of the Carnegie Ridge segment is not flat, but regularly dipping at an angle of 25° (see also Lonsdale, 1978; Pennington, 1981; Prévot *et al.*, 1996) although immediately to the north the dip increases slightly to 30° leaving open the possibility of a slab tear.

Three distinct trench-parallel chains of volcanoes occur in Ecuador (Fig. 2a): (1) a frontal arc chain in the western Cordillera including volcanic centers such as Pilavo, Cotacachi–Cuicocha, Pululahua, Pichincha, Atacazo, Corazon and Illiniza; (2) a main volcanic arc chain on the western margin of the Eastern Cordillera including the volcanic centers of Cayambe, Chacana, Antisana, Cotopaxi, Tungurahua and Sangay; (3) a back-arc chain including the volcanic centers of Reventador, Pan de Azucar, Sumaco and Puyo. Between the frontal and the main arc several volcanoes also occur in the Interandean Valley, such as Cusin, Mojanda and Ilalo (Fig. 2a). The crustal thickness beneath the Eastern Cordillera, where Chacana is situated, is >50 km based on gravimetric data (Feininger & Seguin, 1983) or 50–75 km based on seismic data (Guillier *et al.*, 2001).

Various studies have shown systematic geochemical changes in the compositions of the lavas of the Ecuadorian arc from the frontal-arc to the back-arc region (Barragan *et al.*, 1998; Bourdon *et al.*, 2003; Bryant *et al.*, 2006; Chiaradia *et al.*, 2009). These variations have been interpreted as the result of progressively smaller amounts of partial melting of the mantle wedge metasomatized by a slab component towards the back-arc (K–h relationship: Dickinson, 1975). Rocks considered to be equivalent to slab melts, often called adakites (Defant & Drummond, 1990), have distinctive geochemical characteristics, such as high Sr/Y and La/Yb values (Kay, 1978; Defant & Drummond, 1990; Martin *et al.*, 2005). Some of the Quaternary Ecuadorian volcanic arc rocks have such geochemical signatures. The question is, however, whether the adakite-like signatures of the Quaternary Ecuadorian rocks reflect melting of the subducted slab (e.g. Gutscher *et al.*, 1999, 2000; Samaniego *et al.*, 2002; Bourdon *et al.*, 2003) or are the result of lower to mid-crustal magmatic processes (Kilian *et al.*, 1995; Arculus *et al.*, 1999; Garrison & Davidson, 2003; Chiaradia *et al.*, 2004, 2009, 2011; Bryant *et al.*, 2006; Garrison *et al.*, 2006; Chiaradia, 2009) as has been suggested to be the case elsewhere, and in the Central Andes in particular (e.g. Atherton & Petford, 1993).

LOCAL GEOLOGICAL SETTING

Chacana is an eroded, Plio-Holocene caldera complex forming one of the largest rhyolitic centers of the northern Andes (32 km in the north–south direction and 18–24 km in the east–west direction: Global Volcanism Program, http://www.volcano.si.edu/; Fig. 2a and b). It is located in the Eastern Cordillera (Fig. 2a) upon the basement of the Loja continental terrane (Paleozoic gneisses and schists as well as Triassic granites) and of the Alao island arc terrane (Jurassic meta-basalts) (Aspden & Litherland, 1992; Litherland *et al.*, 1994; Noble *et al.*, 1997). The Chacana caldera consists of four main lithological groups according to Hall & Mothes (2008). The oldest (2·5–2·7 Ma) is a belt of

dikes and fault-related breccias representing the inferred ring fracture of the eastern margin of the caldera (Fig. 2b). The second group consists of a >1250 m thick sequence of dacitic to rhyolitic ignimbrites and tuffs with intercalations of subordinate andesitic to dacitic lavas (2·7–0·22 Ma), which cover the western flank of the caldera before disappearing under the Inter-Andean Valley sediments (Fig. 2b). An 8 m thick pumice fall unit and a 7 km long obsidian flow overlying the above sequence were dated at 0·16–0·17 Ma (Hall & Mothes, 2008). The third group is the caldera-infilling consisting of tuff, breccia, porphyritic andesitic lavas (1·5–1·9 Ma), and a fluvial detrital sequence made up of volcanic clasts (Fig. 2b). The fourth group consists of andesitic to dacitic lava flows several kilometers long, erupted from vents aligned along a NNE trend in the western part of the caldera (not shown in Fig. 2b, but all sample locations in it are from such flows). These flows (hereafter termed Young Chacana) have ages mostly ranging from 0·45 to 0·16 Ma, but more recent lavas also erupted between 30 and 20 ka and the latest andesitic flows are from AD 1700 (Hall & Mothes, 2008). The investigated sanukitoid-like lava flow (named

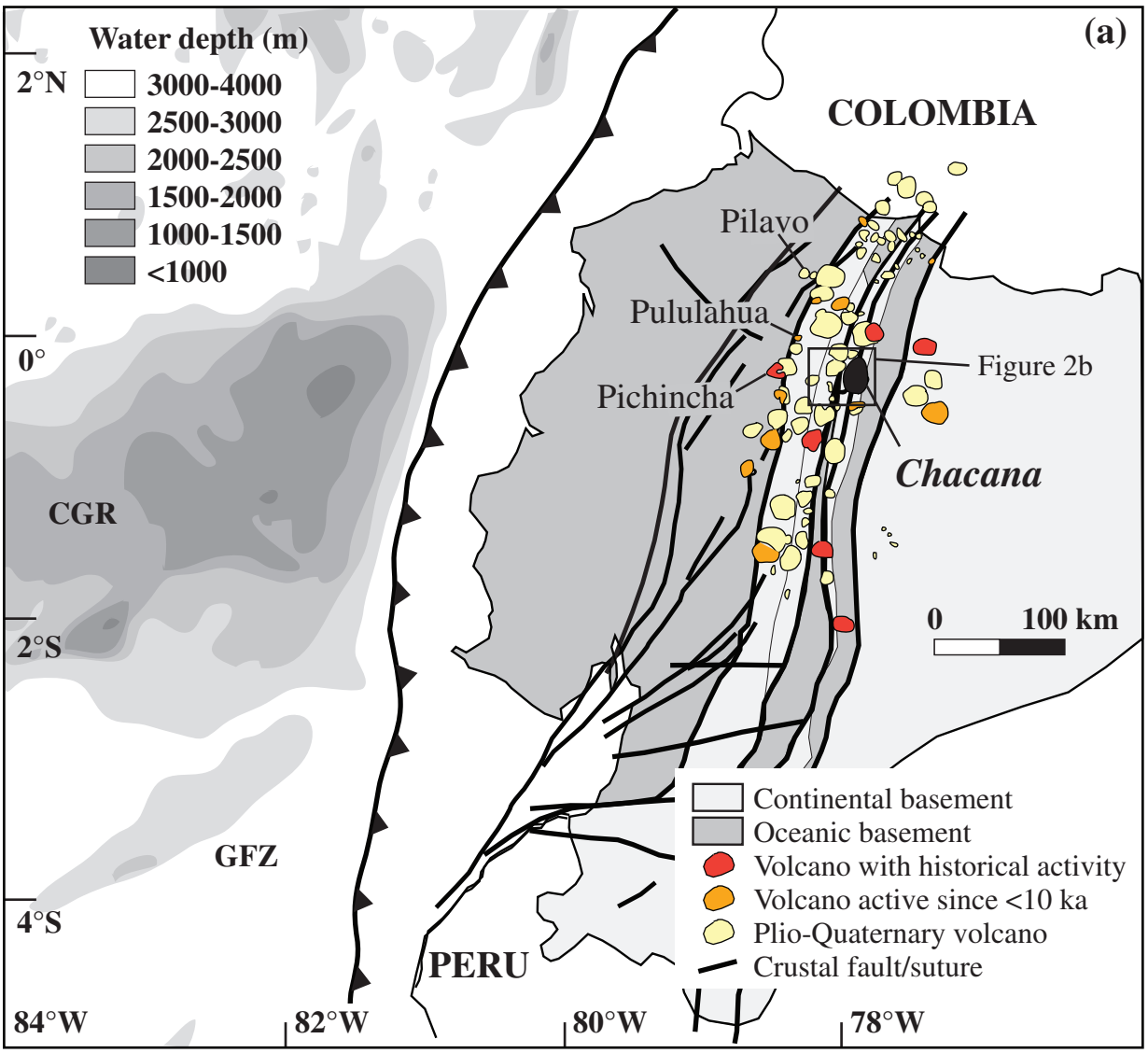

Fig. 2. (a) Map of Ecuador showing the main topographic features of the subducting plate (CGR, Carnegie Ridge; GFZ, Grijalva Fracture Zone) and location of recent and active volcanoes of Ecuador (modified after Litherland *et al.*, 1994; Corredor, 2003). (b) Topographic map of the Chacana caldera with superimposed main geological features (from Hall & Mothes, 2008) and location of samples of andesite lava flows erupted in the latest stage of the caldera (<0·45 Ma to AD 1700). The Yuyos sanukitoid-like lava flow corresponds to samples 22-3-4 and 1202 to 1207.

(continued)

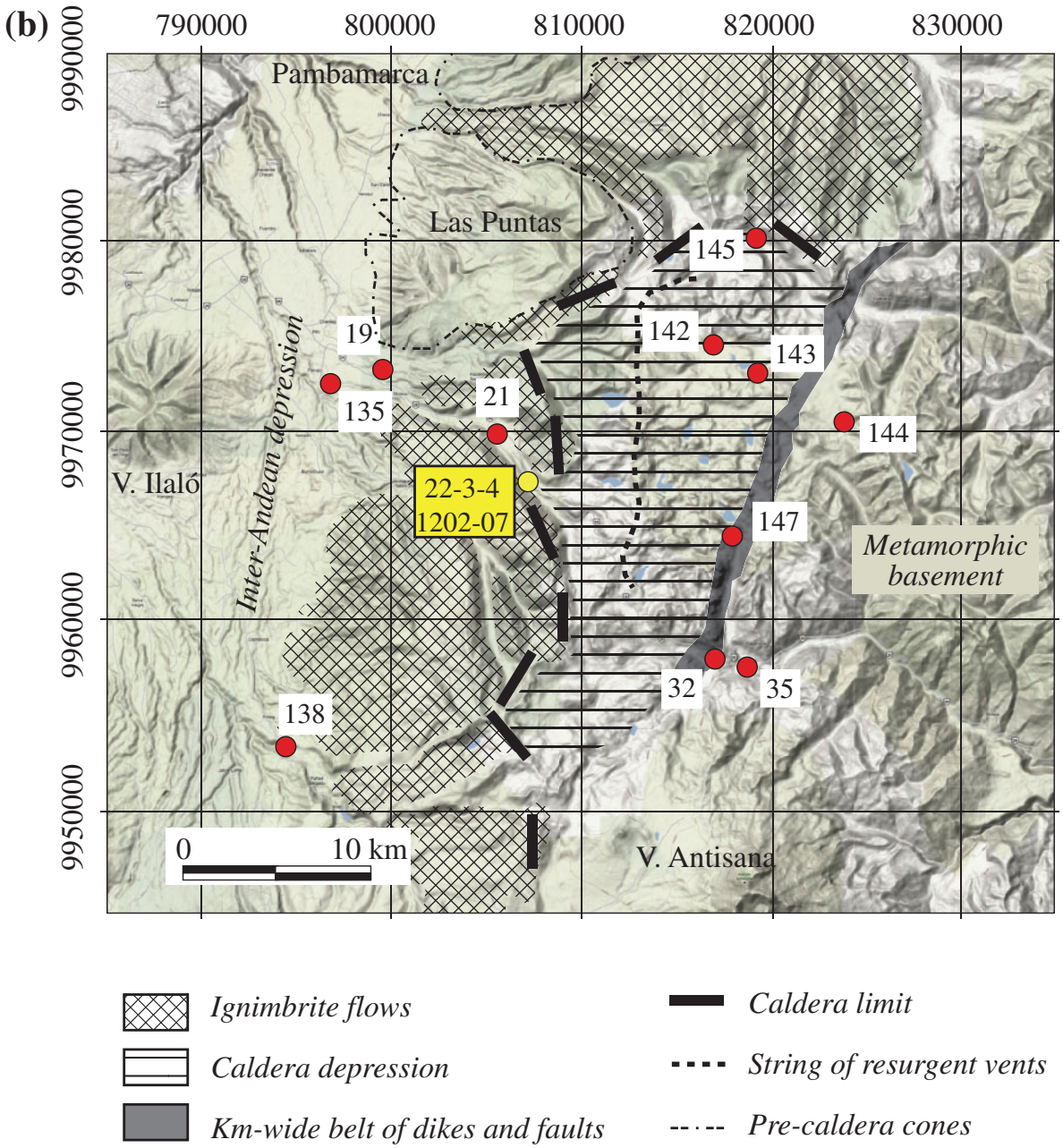

Fig. 2. Continued.

Yuyos) represents one of these flows (Fig. 2b) and has an age of ~30 ka (M. L. Hall, personal communication). The flow is >4 km long, 100–300 m wide and at the front reaches a thickness of ~30 m. We have collected and analysed nine samples from a road-cut section of the flow over a distance of 1300 m.

ANALYTICAL METHODS

Microprobe analyses of amphibole, pyroxene, olivine and volcanic glass (Supplementary Data Table, available for downloading at http://www.petrology.oxfordjournals.org) were carried out using a JEOL 8200 microprobe at the Institute of Earth Sciences, University of Lausanne, equipped with five wavelength-dispersive spectrometers. Analytical conditions were sample current 15 or 20 nA, acceleration voltage 15 kV, measuring time 10–30 s on peak, and half the time on the respective backgrounds depending on the element, and a spot size of 1–5 μm depending on the element and mineral. Both natural and synthetic silicate, oxide, and sulfate standards were used for external calibration. A CitZaf correction

procedure (developed by J. T. Armstrong, Caltech, 1988) was applied to the raw data.

In situ trace and rare earth element (REE) analyses of volcanic glasses were carried out on polished thin sections by laser ablation inductively coupled plasma mass spectrometry (LA-ICP-MS) using a Perkin Elmer ELAN 6100 DRC ICP-MS system equipped with a 193 nm EXCIMER Geolas laser at the University of Lausanne. Operating conditions of the laser were 8 Hz frequency, 100 mJ energy and 60 μm spot size. CaO contents determined by microprobe in the area of subsequent ablation with the laser were used for internal standardization by reference to an SRM612 NIST external standard. Raw data were reduced off-line using the LAMTRACE software (Jackson *et al.*, 1992; Longerich *et al.*, 1996; Jackson, 2008).

Whole-rock samples (Table 1 and Fig. 2b) were analyzed for major and trace elements by X-ray fluorescence (XRF) at Lausanne University (Switzerland). REE and additional trace elements (e.g. Th, U, Ta, Cs, Hf) were measured by LA-ICP-MS on the fused glass beads used for major element XRF analysis using the same LA-ICP-MS instrument as for minerals (Table 1). Operating conditions of the laser were 10 Hz frequency, 140 mJ energy and 120 μm spot size. CaO contents previously determined by XRF were used for internal standardization by reference to an SRM612 NIST external standard. Raw data were reduced off-line using the LAMTRACE software.

The whole-rocks were investigated for their Sr, Nd and Pb isotopic compositions at the Department of Mineralogy, University of Geneva (Table 1). About 130 mg of powdered rock fractions (<70 μm) were dissolved in closed Teflon vials over 7 days on a hot plate at 140°C with a mixture of 4 ml concentrated HF and 1 ml 15M HNO_3. The sample was then dried on a hot plate and dissolved in 3 ml 15M HNO_3 in closed Teflon vials at 140°C and dried down again. Sr, Nd and Pb separation was carried out using cascade columns with Sr-spec, TRU-spec and Ln-spec resins, following a modified method after Pin *et al.* (1994). Pb was further purified with AG-MP1-M anion exchange resin in a hydrobromic medium.

Pb, Sr and Nd isotope ratios were measured on a Thermo TRITON mass spectrometer at the University of Geneva (Switzerland). Pb was loaded on Re filaments using the silica gel technique (Gerstenberger & Haase, 1997) and all samples (and standards) were measured at a pyrometer-controlled temperature of 1220°C on Faraday cups in static mode. Pb isotope ratios were corrected for instrumental fractionation by a factor of 0·07% per a.m.u. based on more than 90 measurements of the SRM981 standard and using the standard values of Todt *et al.* (1996). External reproducibility of the standard ratios is 0·08% for $^{206}Pb/^{204}Pb$, 0·12% for $^{207}Pb/^{204}Pb$ and 0·16% for $^{208}Pb/^{204}Pb$.

Sr was loaded on single Re filaments with a Ta oxide solution and measured at a pyrometer-controlled temperature of 1480°C in static mode using the virtual amplifier design to cancel out biases in gain calibration among amplifiers. $^{87}Sr/^{86}Sr$ values were internally corrected for fractionation using a $^{88}Sr/^{86}Sr$ value of 8·375209. Raw values were further corrected for external fractionation by a value of +0·03‰, determined by repeated measurements of the SRM987 standard ($^{87}Sr/^{86}Sr = 0·710248$). External reproducibility of the $^{87}Sr/^{86}Sr$ ratio for the SRM987 standard is 7 ppm. Nd was loaded on double Re filaments with 1 M HNO_3 and measured in static mode with the virtual amplifier design. $^{143}Nd/^{144}Nd$ values were internally corrected for fractionation using a $^{146}Nd/^{144}Nd$ value of 0·7219 and the ^{144}Sm interference on ^{144}Nd was monitored on the mass ^{147}Sm and corrected by using a $^{144}Sm/^{147}Sm$ value of 0·206700. These values were further corrected for external fractionation by a value of +0·03‰, determined by repeated measurements of the JNdi-1 standard ($^{143}Nd/^{144}Nd = 0·512115$; Tanaka *et al.*, 2000). External reproducibility of the JNdi-1 standard is <5 ppm.

RESULTS

Petrography and bulk-rock geochemistry

The Young Chacana 'normal' andesitic lavas contain abundant plagioclase and pyroxene ± amphibole ± olivine phenocrysts. In contrast, the Yuyos lava flow is dark grey to blackish in colour, very fine-grained, with a small number of pheno- or xenocrysts (<15%) represented by olivine, clinopyroxene, and heavily to completely corroded amphibole and biotite (see Table 2 and Figs 3–5). Olivine occurs as sub- to idiomorphic apparently equilibrium phenocrysts [type (i): Fig. 3a and b], as xenocrysts with opacite rims [type (ii): Fig. 3c] or as xenocrysts surrounded by amphibole coronae [type (iii): Fig. 3d]. Olivine may occur as isolated crystals or as glomerocrysts, and sometimes shows wavy extinction. Clinopyroxene occurs as equilibrium idiomorphic phenocrysts with or without inclusions in their cores [type (i): Fig. 3e and f], acicular to stubby phenocrysts around glass globules and quartz xenocrysts [type (ii): Fig. 3g], and as large dusty xenocrysts with inverse zoning [type (iii): Fig. 3h]. Amphibole and biotite phenocrysts, in addition to being heavily corroded, have thick plagioclase–pyroxene–Fe–Ti oxide (gabbroic-type) and/or opacitic (Fe–Ti-oxides) rims (several tens of micrometers). In some cases, amphiboles are also patchily or completely replaced by a coarse-grained assemblage of pyroxene, plagioclase and Fe–Ti oxides (Fig. 4a–f). Some amphibole cores are also replaced by melt (glass: Fig. 5d). Very rare relic plagioclase phenocrysts (2–3 per thin section) have been observed (Fig. 4g). The groundmass consists of plagioclase microlites and glass plus subordinate amounts of pyroxene and olivine in a glassy matrix (Figs 3–5). A typical petrographic feature of the Yuyos andesites is the occurrence of relatively large

Table 1: Major and trace element and Sr–Nd–Pb isotopic compositions of Yuyos whole-rocks

Coord.:	0°17′46″S, 78°14′25″W			0°17′49″S, 78°14′43″W	0°17′45″S, 78°14′26″W				0°18′4″S, 78°14′3″W
Sample:	E05022	E05023	E05024	E12002	E12003	E12004	E12005	E12006	E12007
Rock:	Andesite	Basaltic andesite	Basaltic andesite	Basaltic andesite	Basaltic andesite	Basaltic andesite	Basaltic andesite	Basaltic andesite	Basaltic andesite
SiO_2	57·2	56·3	55·8	56·4	56·2	56·3	56·4	56·1	55·9
TiO_2	0·68	0·71	0·73	0·74	0·75	0·74	0·73	0·74	0·75
Al_2O_3	15·2	15·3	16·0	16·0	16·2	16·0	15·5	16·0	16·0
Fe_2O_3	6·97	7·12	7·14	7·21	7·29	7·23	7·17	7·25	7·33
MnO	0·12	0·12	0·12	0·12	0·12	0·12	0·12	0·12	0·12
MgO	5·91	5·87	4·98	5·17	5·24	5·24	5·71	5·23	5·26
CaO	7·34	7·58	7·54	7·5	7·59	7·49	7·6	7·54	7·55
Na_2O	3·35	3·41	3·51	3·24	3·23	3·27	3·11	3·27	3·23
K_2O	2·84	2·84	2·95	2·84	2·88	2·84	2·81	2·84	2·86
P_2O_5	0·41	0·41	0·4	0·5	0·51	0·5	0·5	0·5	0·51
LOI	0·14	0·39	0·15	-0·04	0·18	0	0·16	0·1	-0·04
Total	100·3	100·2	99·5	99·7	100·1	99·7	99·8	99·7	99·5
Rb	60·5	59·3	58·4	60·2	60·5	60·1	61·8	59	59·7
Sr	1429	1493	1555	1545	1565	1546	1495	1543	1561
Y	19·5	19·6	20·5	19·7	19·7	19·7	19·2	19·7	19·9
Zr	215	219	220	203	205	204	210	202	204
Nb	5·7	5·6	5·7	5·3	5·2	5·2	5·6	5·2	5·2
Cs	2·53	1·99	2·12	2·5	2·8	2·5	2·4	2·5	1·7
Be	3·64	3·41	3·08	n.m.	n.m.	n.m.	n.m.	n.m.	n.m.
Ba	1593	1585	1664	1746	1763	1746	1637	1740	1795
Hf	3·49	4·68	3·29	4	4	4	4	4	4
Ta	0·43	0·61	0·4	n.m.	n.m.	n.m.	n.m.	n.m.	n.m.
Pb	19·5	13·4	15·8	17	23	18	16	18	19
Th	17·1	22·5	17·8	20	20·1	21·1	18·7	19·1	19·9
U	5·8	6·5	6·6	7·4	7·0	6·9	6·3	6·6	6·8
Sc	22·4	25·3	22·5	n.m.	n.m.	n.m.	n.m.	n.m.	n.m.
V	158	163	170	173	177	174	173	174	175
Cr	75	85	44	38	37	37	77	41	36
Ni	47	46	26	30	32	31	44	30	31
Cu	92	78	69	43	51	54	36	66	65
Co	27·0	27·0	25·0	27·3	26·6	26·8	27·3	26·1	26·7
Zn	80	77	77	78	82	78	79	81	81
La	73·8	94·1	80·6	87·8	87·5	87·7	83·8	86·6	89·3
Ce	144·6	161·9	157·0	167·0	167·0	168·0	161·0	165·0	169·0
Pr	16·9	19·6	18·3	20·5	20·3	20·4	19·6	20·4	20·6
Nd	68·3	80·6	73·2	80·0	79·6	79·2	77·5	77·9	79·7
Sm	11·1	13·9	11·9	12·7	13·1	12·8	12·6	13·3	12·8
Eu	2·78	3·24	3·02	3·10	2·99	3·03	3·00	3·11	3·14
Gd	6·94	9·48	7·36	8·11	8·08	7·96	7·95	8·07	8·35
Tb	0·74	0·95	0·78	1·01	0·99	1·00	0·97	0·97	0·95
Dy	3·73	5·20	4·02	4·42	4·38	4·34	4·15	4·23	4·31
Ho	0·63	0·87	0·65	0·72	0·72	0·69	0·68	0·72	0·7
Er	1·61	2·16	1·67	1·96	1·93	1·91	1·97	1·7	1·8

(continued)

Table 1: Continued

Coord.:	0°17′46″S, 78°14′25″W			0°17′49″S, 78°14′43″W	0°17′45″S, 78°14′26″W				0°18′4″S, 78°14′3″W
Sample:	E05022	E05023	E05024	E12002	E12003	E12004	E12005	E12006	E12007
Rock:	Andesite	Basaltic andesite	Basaltic andesite	Basaltic andesite	Basaltic andesite	Basaltic andesite	Basaltic andesite	Basaltic andesite	Basaltic andesite
Tm	0·23	0·29	0·25	0·23	0·26	0·26	0·24	0·23	0·22
Yb	1·55	2·01	1·44	1·70	1·50	1·60	1·60	1·50	1·60
Lu	0·21	0·28	0·22	0·29	0·27	0·26	0·22	0·25	0·25
Mg-no.	0·63	0·62	0·58	0·58	0·59	0·59	0·59	0·61	0·59
$^{87}Sr/^{86}Sr$	0·703949	0·703917	0·703943	0·703967	0·703951	0·703961	0·703941	0·703939	0·703944
$^{143}Nd/^{144}Nd$	0·513030	0·512926	0·512952	0·512966	0·512962	0·512962	0·512965	0·512967	0·512968
ε_{Nd}	7·7	5·6	6·1	6·4	6·3	6·3	6·4	6·4	6·4
$^{206}Pb/^{204}Pb$	19·03	19·05	19·02	19·04	19·02	19·04	19·02	19·03	19·02
$^{207}Pb/^{204}Pb$	15·62	15·63	15·62	15·63	15·61	15·64	15·60	15·62	15·60
$^{208}Pb/^{204}Pb$	38·75	38·78	38·76	38·81	38·75	38·82	38·72	38·78	38·71

n.m., not measured.

quartz xenocrysts (usually several tens to hundreds of micrometers, but in some cases up to millimeters and even >1 cm) surrounded by dark brown to whitish (closer to quartz) glass and an outward corona of acicular to stubby clinopyroxene (Fig. 4h). Interstitial melts and melt inclusions are found within different phenocrysts and associated with mineral clots in different textural positions (Table 2; Figs 3 and 5; Supplementary Data Table). The Yuyos lava flow shows similar petrographic features to lavas of the Miocene Setouchi volcanic belt, Japan (Tatsumi, 2006).

The Yuyos lava flow has a basaltic trachyandesite to trachyandesite composition as opposed to the typical andesitic composition of the Young Chacana (YC) rocks (Fig. 6a). It has the lowest SiO_2 and Na_2O and the highest MgO, Fe_2O_{3tot}, CaO and K_2O contents of all Chacana andesites, and is characterized by high Mg# [molar $Mg/(Mg + Fe_{tot}) = 0{\cdot}58$–$0{\cdot}63$: Table 1]. Compared with the normal Young Chacana andesites and to other Ecuadorian frontal arc volcanoes (Pichincha and Pululahua) with the lowest SiO_2 contents (comparable with those of the Yuyos andesites) it has significantly lower Ni and Cr contents (Fig. 7). In contrast, the Yuyos andesites, like the Pilavo frontal arc volcano, have higher contents of many incompatible trace elements (notably Th, U, Ba, Sr and La; Fig. 7) than any other rock of Young Chacana, Pululahua and Pichincha.

The REE patterns of the Yuyos andesites, despite having a similar shape to those of the Young Chacana andesites (Fig. 8), with significant fractionation between light REE (LREE) and heavy REE (HREE), a nearly flat to slightly declining pattern between Dy and Lu, and no Eu negative anomaly, display higher absolute values of all REE. Primitive mantle-normalized trace element patterns are markedly different between the Yuyos and Young Chacana andesites. Whereas both are characterized by Nb negative anomalies, the Yuyos andesites are strongly enriched in many LILE and HFSE such as Ba, Th, Pb, Sr and REE, and moderately enriched in K, but have similar values of P, Zr and Ti, resulting in negative anomalies of these elements compared with the adjacent REE.

The Yuyos andesites have more depleted Sr ($^{87}Sr/^{86}Sr$ 0·70390–0·70395) and Nd ($\varepsilon Nd_0 = +5{\cdot}5$ to $+7{\cdot}8$) isotopic compositions than the Young Chacana andesites ($^{87}Sr/^{86}Sr$ 0·70422–0·70437; εNd_0 $+1{\cdot}5$ to $+3{\cdot}3$), which are amongst the most depleted of all Quaternary Ecuadorian volcanic rocks (only the frontal arc Pilavo volcano has been found to have similar signatures so far: $^{87}Sr/^{86}Sr$ 0·70375–0·7039; εNd_0 $+5{\cdot}5$ to $+6{\cdot}2$; Fig. 9). In terms of Pb isotopes the Yuyos andesites are also more akin to the frontal arc Pilavo volcano than to the Young Chacana normal andesites, being characterized by generally higher $^{206}Pb/^{204}Pb$ values at similar (but more restricted) $^{207}Pb/^{204}Pb$ and $^{208}Pb/^{204}Pb$ values (Fig. 9).

Mineral chemistry

Olivine

The mineral chemistry of olivine reflects to some extent its textural variations (Table 2; Fig. 3; full dataset is given in the Supplementary Data Table). Olivine cores have forsterite contents between 81 and 88 (Fig. 10a), with the highest forsterite contents (Fo86–88) in type (iii), associated with amphibole. Forsterite and NiO contents are highly variable

Table 2: Textural types of minerals and interstitial melts

Olivine	Clinopyroxene
(i) Sub-idiomorphic ± fragmented olivine, characterized by more or less rounded to corroded rims at the contact with the groundmass (Fig. 3a and b). This olivine type occurs sometimes as angular fragments and includes olivine with spongy cellular textures and groundmass olivine	(i) Apparently equilibrium idiomorphic and clear clinopyroxenes with concentric optical zoning and sometimes with wormy glass inclusions in the core (Fig. 3e and f)
(ii) Reacted olivine with resorbed sinuous shapes and variably thick opaque oxide rims at the contact with the groundmass (Fig. 3c)	(ii) Stubby to acicular clinopyroxenes around glass pockets and quartz xenocrysts (Fig. 3g)
(iii) Olivine surrounded by a corona of amphibole or in contact association with opacitized amphibole (Fig. 3d)	(iii) Variably large clinopyroxenes with dusty cores forming disequilibrium clots surrounded by opacite and glass and containing in their interior abundant glass (Fig. 3h)
Amphibole	**Plagioclase**
(i) Amphibole associated with olivine and surrounded by a thick opacite rim (Fig. 3d)	(i) Rare interstitial, apparently newly crystallized, phase in glass pockets sheltered by other phenocrysts (e.g. opacitized amphibole)
(ii) Amphibole associated with clinopyroxene and surrounded by a thick opacite rim	(ii) Extremely rare microcrysts that are variably rounded and heavily sieved on the outer rims (Fig. 4g)
(iii) Isolated, zoned amphibole highlighted by opacite layers separating different growth zones within amphibole (Fig. 4a and b)	(iii) Microlites in the glass groundmass (Figs 3–5)
(iv) Homogeneous isolated amphibole without zoning (Fig. 4c)	
Interstitial melts	
(i) In the groundmass, interstitial to plagioclase microlites (volcanic glass) (Figs 3–5)	
(ii) Large (tens to hundreds of μm) interstitial pockets associated with clinopyroxene and olivine (Fig. 5a and b)	
(iii) Melt inclusions inside olivine, amphibole and clinopyroxene phenocrysts (Fig. 5c and d)	
(iv) Blebs frequently dispersed in the groundmass and surrounded by a thin corona of acicular to stubby clinopyroxene (Fig. 5e and f), which might have an empty bubble in the middle (Fig. 5e)	
(v) Glass surrounding quartz xenocrysts and in turn surrounded by a clinopyroxene corona as in type (iv) (Fig. 4h)	

from core to rim, ranging from roughly flat profiles to normal and inverse zoning. Normal forsterite and NiO zoning is the dominant pattern found in type (i) olivine (Fig. 10b). The forsterite content variability between olivine cores and rims is negatively correlated with both olivine phenocryst size and the (maximum) forsterite core content (Fig. 10c and d), indicating that low-forsterite olivine is smaller, and displays smoother core to rim profiles (Fig. 10b). Type (ii) olivine shows dominantly flat core to rim profiles of forsterite and NiO content with small compositional changes between cores and rims (Fig. 10e). Two adjacent type (i) and (ii) olivine phenocrysts in sample E05023.3l show distinct forsterite core contents [Fo85: type (i); Fo82·6: type (ii)] with opposite normal [type (i)] and inverse [type (ii)] zoning converging towards a uniform rim composition (~Fo83·5) (Fig. 3b). Disequilibrium type (iii) olivine is characterized by variable core compositions: olivines with more forsterite-rich cores (Fo86–88) display flat to normal zoning whereas olivines with forsterite-poorer cores (Fo83–84) display flat to inverse forsterite and NiO zoning (Fig. 10f).

NiO varies very little with increasing forsterite content and remains generally well below the mantle olivine array (Fig. 10g), suggesting that these olivines crystallized

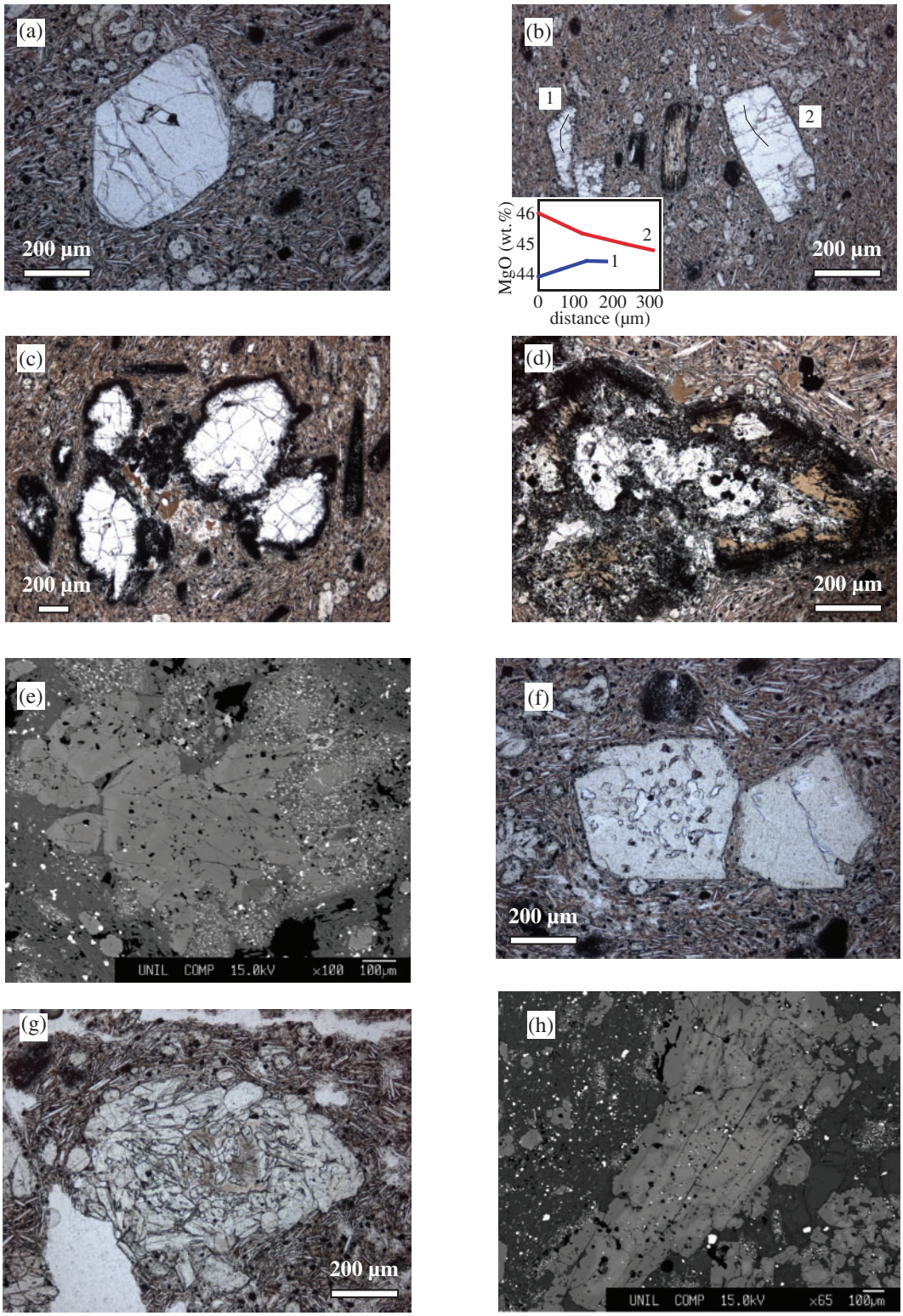

Fig. 3. Photomicrographs of textural types of olivine and clinopyroxene occurring in the Yuyos andesite: (a) subidiomorphic olivine with slightly rounded corners; (b) subidiomorphic olivine with thin oxide rim (right) and angular heavily reacted grain (left), showing (inset) opposite MgO core-to-rim zoning profiles; (c) olivine with thick opacite rims; (d) olivine surrounded by a corona of amphibole with opacitic rim; (e) BSE image of a clinopyroxene with normal zoning (lighter-coloured, Fe-richer rim); (f) idiomorphic clinopyroxene with cellular spongy (vermicular) texture at the core (left) together with idiomorphic inclusion-free clinopyroxene (right); (g) stubby to acicular clinopyroxene growing inside and almost occluding a glass globule; (h) BSE image of a large clinopyroxene with inverse MgO (Cr, Ni) zoning (note the darker, Mg-richer rim, more developed on the outer, left side of the large clinopyroxene).

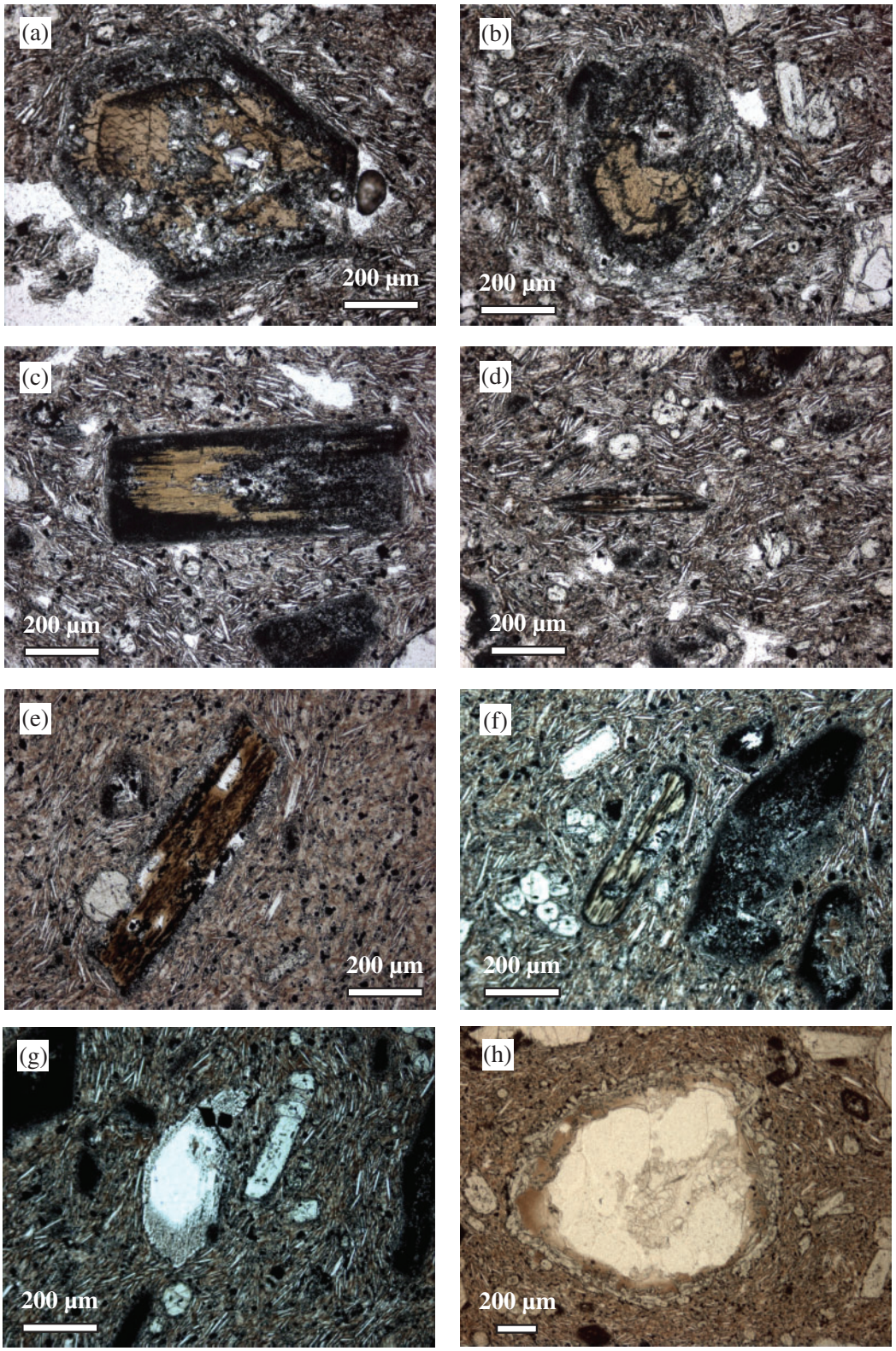

Fig. 4. Photomicrographs of amphibole, biotite, plagioclase and quartz pheno- or xenocrysts: (a, b) amphibole with subsequent growth zones highlighted by internal opacitic rims and thick plagioclase–pyroxene–Fe–Ti oxide (gabbroic-type) rims; (c) apparently homogeneous amphibole with thick opacitic rim; (d) decoloured biotite xenocryst with thick opacitic rim; (e) biotite xenocryst with thick gabbroic-type rim; (f) decoloured biotite with gabbroic-type rim; (g) plagioclase xenocryst with sieve-textured rims; (h) rounded quartz xenocryst with a corona of glass and clinopyroxene.

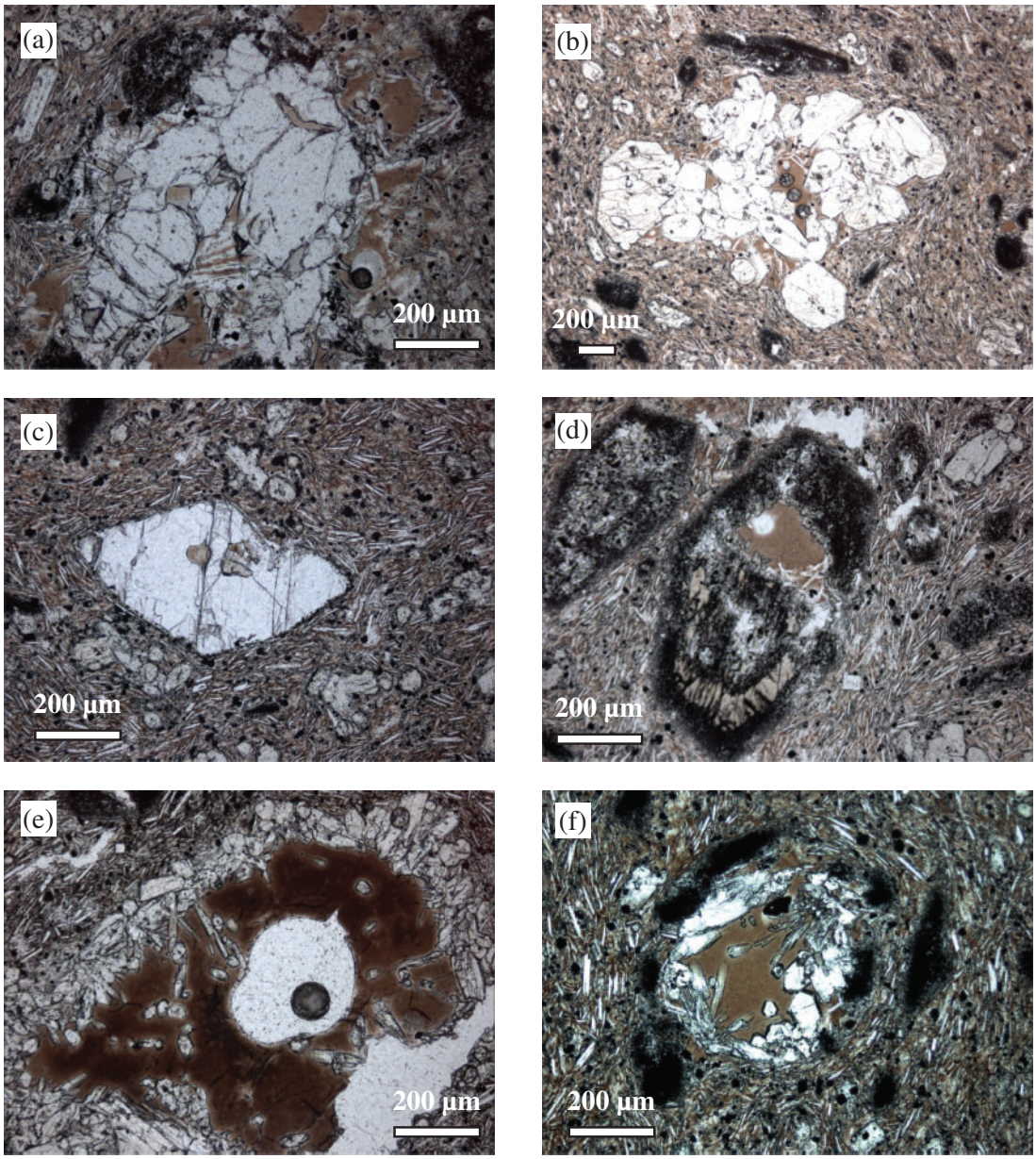

Fig. 5. Photomicrographs of textural types of silicate melts in the Yuyos rocks: (a) interstitial glass associated with olivine; (b) interstitial glass inside a clinopyroxene clot; (c) glass inclusion inside olivine; (d) partly molten core of amphibole; (e) globular glass pocket surrounded by stubby to acicular clinopyroxene at the contact with the groundmass (note the empty, white, shrinkage bubble at the center of the glass pocket, indicating a high volatile content); (f) glass pocket surrounded by stubby to acicular clinopyroxene and perhaps by a 'phantom' of heavily opacitized amphibole; this could represent a more advanced stage of amphibole melting with respect to that of (d).

from fractionated magmas. Olivine in association with amphibole has a higher NiO content (up to ~0·25 wt %) than the rest of the olivines at comparable forsterite contents.

The Mg# of the melt in equilibrium with olivine, assuming an $(Fe/Mg)_{olivine}/(Fe/Mg)_{melt} = 0{\cdot}3$ (Roeder & Emslie, 1970; Ulmer, 1989), ranges between 0·57 and 0·70. Molar FeO/MgO values of some olivine cores of the three types described above are in disequilibrium with the equivalent molar FeO/MgO values of the host bulk-rocks. In particular, the cores of most type (i) and (ii) olivines occurring in the more MgO-rich rocks are apparently in a disequilibrium relationship with the host-rock, whereas they are in an apparent equilibrium relationship in the less MgO-rich rocks (Fig. 10h). Conversely, some type (iii) olivine cores are in apparent equilibrium with the host MgO-rich rocks, whereas others are in apparent disequilibrium with the less MgO-rich host-rock (Fig. 10h).

Clinopyroxene

Clinopyroxene compositions are reported in the Supplementary Data Table. Type (i) clinopyroxene (Table 2) is characterized by normal MgO zoning or by broadly flat profiles (including slightly normal and slightly inverse MgO patterns: Fig. 11a). Type (iii) clinopyroxene (Table 2) displays inverse MgO profiles with an abrupt increase of MgO from 13·9 ± 0·5 wt % in the cores to 16·6 ± 0·4 wt % in the thin rims (Fig. 11b). The MgO contents of the cores of these clinopyroxenes are the lowest measured among all types, whereas the MgO contents of their rims overlap with core contents of the other clinopyroxene types (16·7 ± 0·7 wt %). Cores of clinopyroxene (iii) also have the highest Na_2O and lowest Cr_2O_3 and NiO contents. The $Mg/(Mg + Fe_{tot})$–Ti plot (Fig. 11c) highlights the distinction between the three types of clinopyroxene, with the type (ii) clinopyroxene (acicular to stubby clinopyroxenes around quartz xenocrysts or glass blebs) being characterized by very low Ti contents and the cores of type (iii) clinopyroxenes having the lowest $Mg/(Mg + Fe_{tot})$.

Clinopyroxenes display a positive correlation between Al^{iv} and Ti (Fig. 11d) and a negative correlation between Al^{iv} and Mn indicative of the *T*-sensitive Ti-Tschermak substitution. The Mg# of the melt in equilibrium with clinopyroxene, assuming an $(Fe/Mg)_{cpx}/(Fe/Mg)_{melt} =$ 0·26–0·30, ranges between 0·28–0·31 and 0·71–0·74.

Amphibole

The analysed amphiboles have Al_2O_3 contents >10 wt % and are mostly magnesio-hastingsite, with minor hornblende and ferri-tschermakite [according to the classification scheme of Leake *et al.* (1997): Supplementary Data Table]. Magnesio-hastingsite may sometimes contain

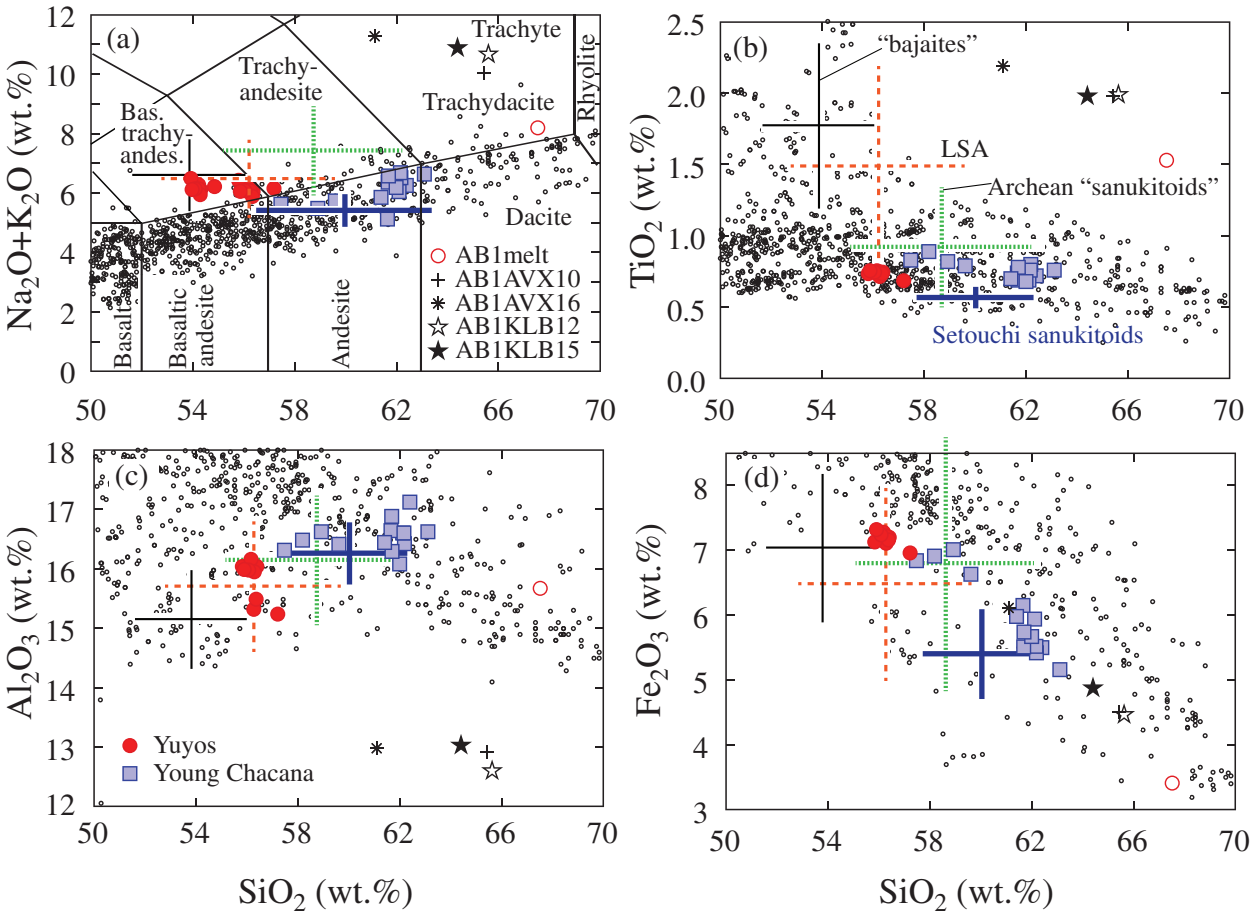

Fig. 6. Silica vs major element variation diagrams for the Yuyos lava flow compared with the 'normal' andesites of Young Chacana. Also plotted are the compositions of low-silica adakites (LSA: Martin *et al.*, 2005), experimental eclogite melt (AB1) and the products of reactions of the latter with peridotite (AB1AVX10, AB1AVX16, AB1KLB12, AB1KLB15: Rapp *et al.*, 1999), Archean sanukitoids (Martin *et al.*, 2010), Setouchi sanukitoids (Shimoda *et al.*, 1998; Tatsumi *et al.*, 2003, 2006), and 'bajaites' (Calmus *et al.*, 2003). Centres of the crosses are average values, length of the arms correspond to 1σ of the population of available values. Small dots correspond to single analyses of enriched high-Mg andesites from the Western Aleutians (Kelemen *et al.*, 2003). Boundaries of rock compositions in (a) are from Le Bas *et al.* (1986).

(continued)

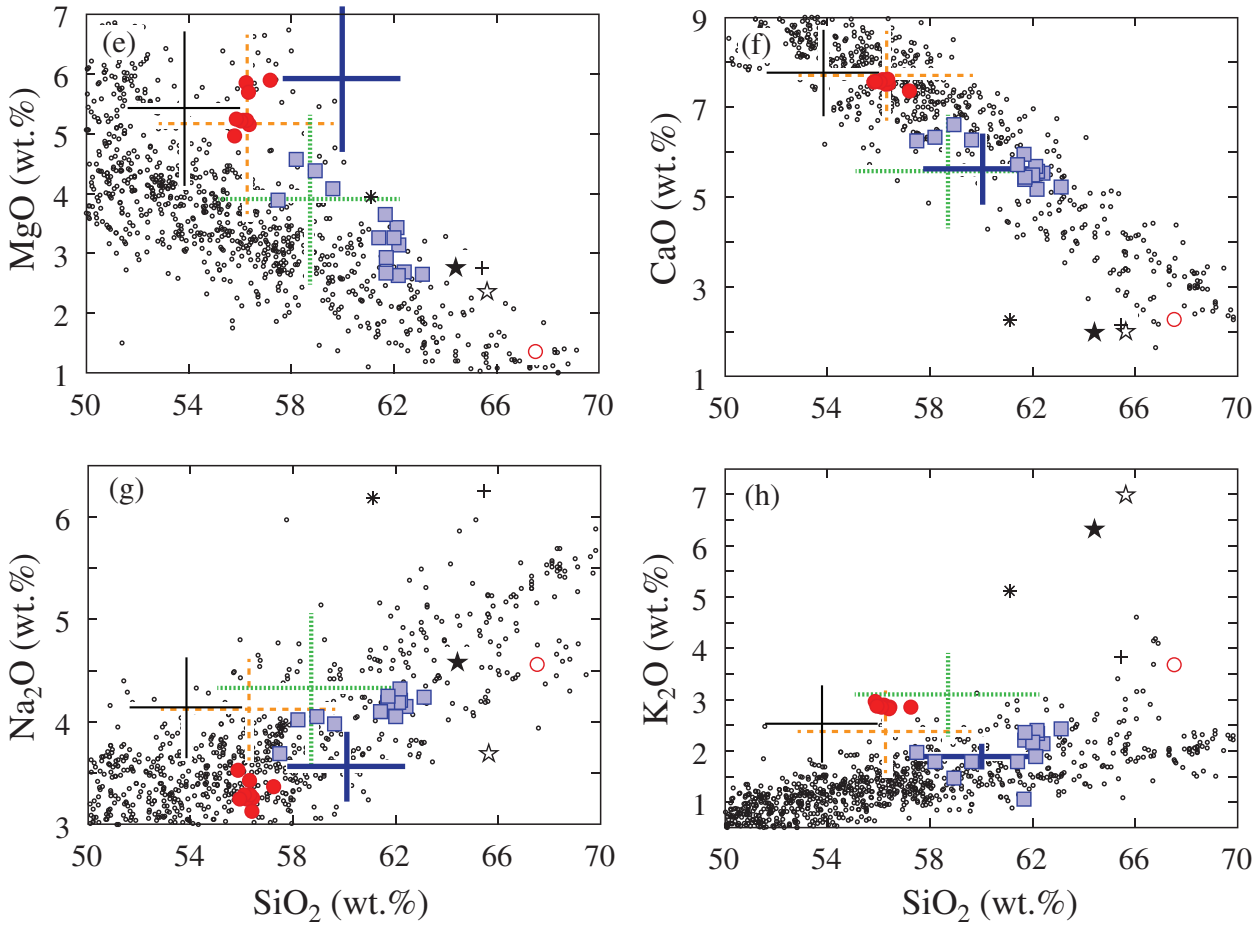

Fig. 6. Continued.

significant amounts of F (up to 2·5 wt % F: fluor-magnesio-hastingsite) and shows rather constant Tschermaks and edenite components (Supplementary Data Table).

The Mg# [Mg/(Mg + Fe_{tot})] of amphibole varies between 0·64 and 0·78 (Fig. 12a). In general, amphibole associated with olivine [type (i)] has the highest Mg# (median = 0·76: Fig. 12a). Amphibole associated with clinopyroxene [type (ii)] has a lower median Mg# (0·72), whereas optically zoned [type (iii)] and homogeneous [type (iv)] amphiboles display a broader range of Mg# with median values of 0·70 and 0·73, respectively. Amphibole compositional zoning is not systematic and both inverse and normal zoning is observed.

Amphiboles do not show pressure-sensitive substitution of Al^{VI} by Al^{IV} (Fig. 12b), nor a pressure-sensitive dependence of Mg# (Fig. 12c), but do show a *T*-sensitive substitution of Ti by Al^{IV} (Fig. 12d).

Pressures calculated using the Ridolfi *et al.* (2010) and Ridolfi & Renzulli (2012) geobarometers (Supplementary Data Table) form a main cluster with a median value of 0·3–0·5 GPa, and a second cluster with a median value of 0·65–0·85 GPa (Fig. 12e). Water contents of the melts in equilibrium with amphibole range between 5 and 10 wt % with a peak at 6–7 wt % (Fig. 12f; Supplementary Data Table).

Biotite

The corroded, opacitized and sometimes decoloured biotite pheno- or xenocrysts are dominated by the phlogopite component (64–78 mol %), with annite (10–16 mol %) and siderophyllite (11–23 mol %) in roughly equal amounts (Supplementary Data Table). A characteristic feature of biotite is its consistently high F content (3·2–5·2 wt %: Supplementary Data Table).

Plagioclase

The anorthite content of plagioclase ranges from 25 to 75 mol % (Fig. 13a and b; Supplementary Data Table). The albite and orthoclase components vary in the range 23–59 mol % and 2–20 mol % respectively. Groundmass plagioclase is low in anorthite (An25-48). Type (i) plagioclase (Table 2) is An50–55, whereas sieved microcrysts [type (ii)] show a broad range between An40 and An75.

The latter show systematic inverse zoning with anorthite-poor cores (from An44 to An60 in the three sieved plagioclases analysed: Fig. 13a and b and Supplementary Data Table) and more anorthite-rich rims (An65–75; Fig. 13a and b and Supplementary Data Table). The same trend is also observed for FeO, with a strong increase at the outer rims (0·58–1·3 wt %) compared with the cores (0·3–0·4 respectively) (Fig. 13a and b and Supplementary Data Table).

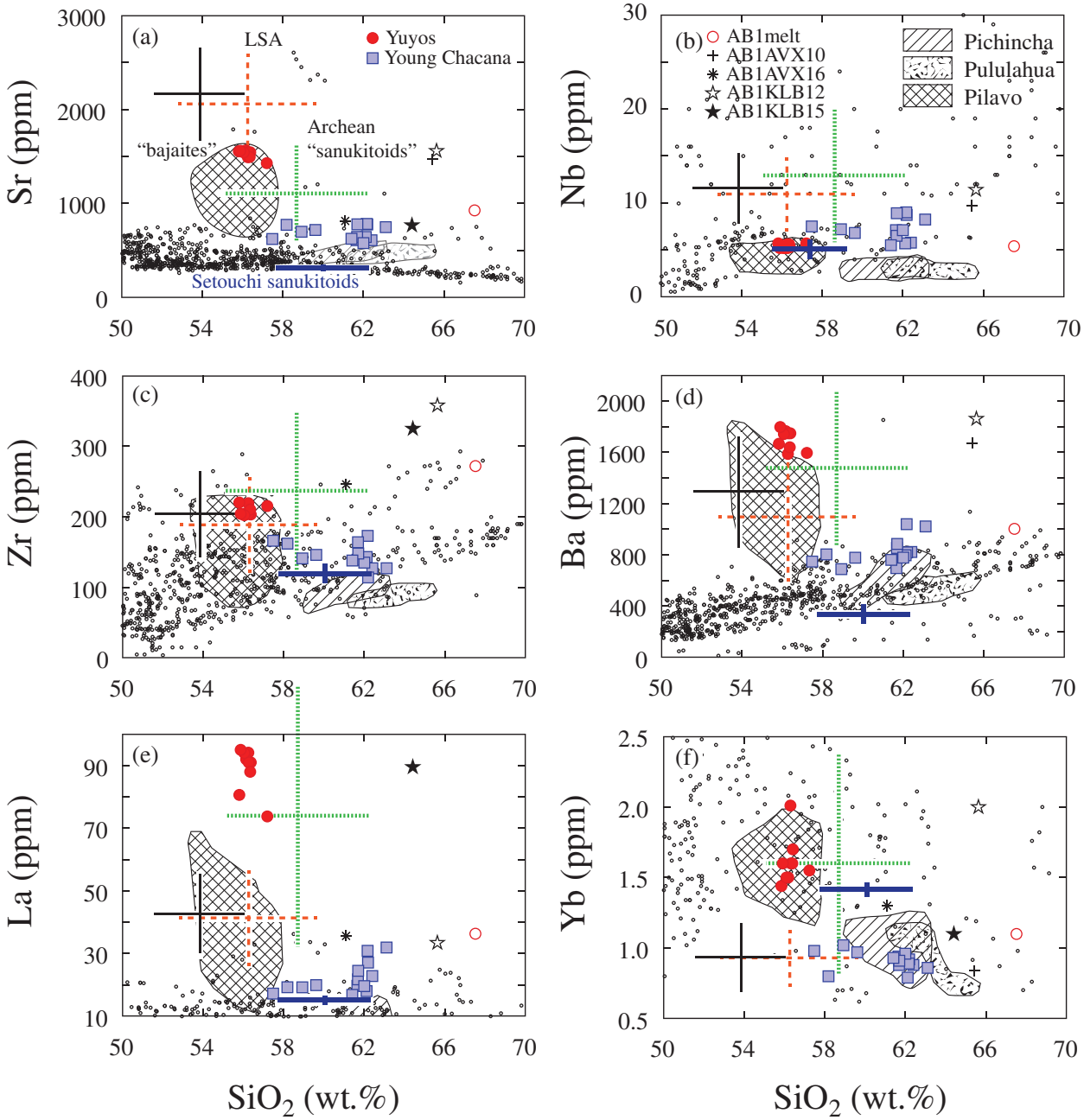

Fig. 7. Silica vs trace element variation diagrams for the Yuyos lava flow compared with the 'normal' andesites of Chacana. Also reported, where data are available, are the compositions of low-silica adakites (LSA: Martin *et al.*, 2005), experimental eclogite melt (AB1) and the products of reactions of the latter with peridotite (AB1AVX10, AB1AVX16, AB1KLB12, AB1KLB15: Rapp *et al.*, 1999), Archean sanukitoids (Martin *et al.*, 2010), Setouchi sanukitoids (Shimoda *et al.*, 1998; Tatsumi *et al.*, 2003, 2006), and 'bajaites' (Calmus *et al.*, 2003). Centres of the crosses are average values, length of the arms correspond to 1σ of the population of available values. Small dots correspond to single analyses of enriched high-Mg andesites from the Western Aleutians (Kelemen *et al.*, 2003).

(continued)

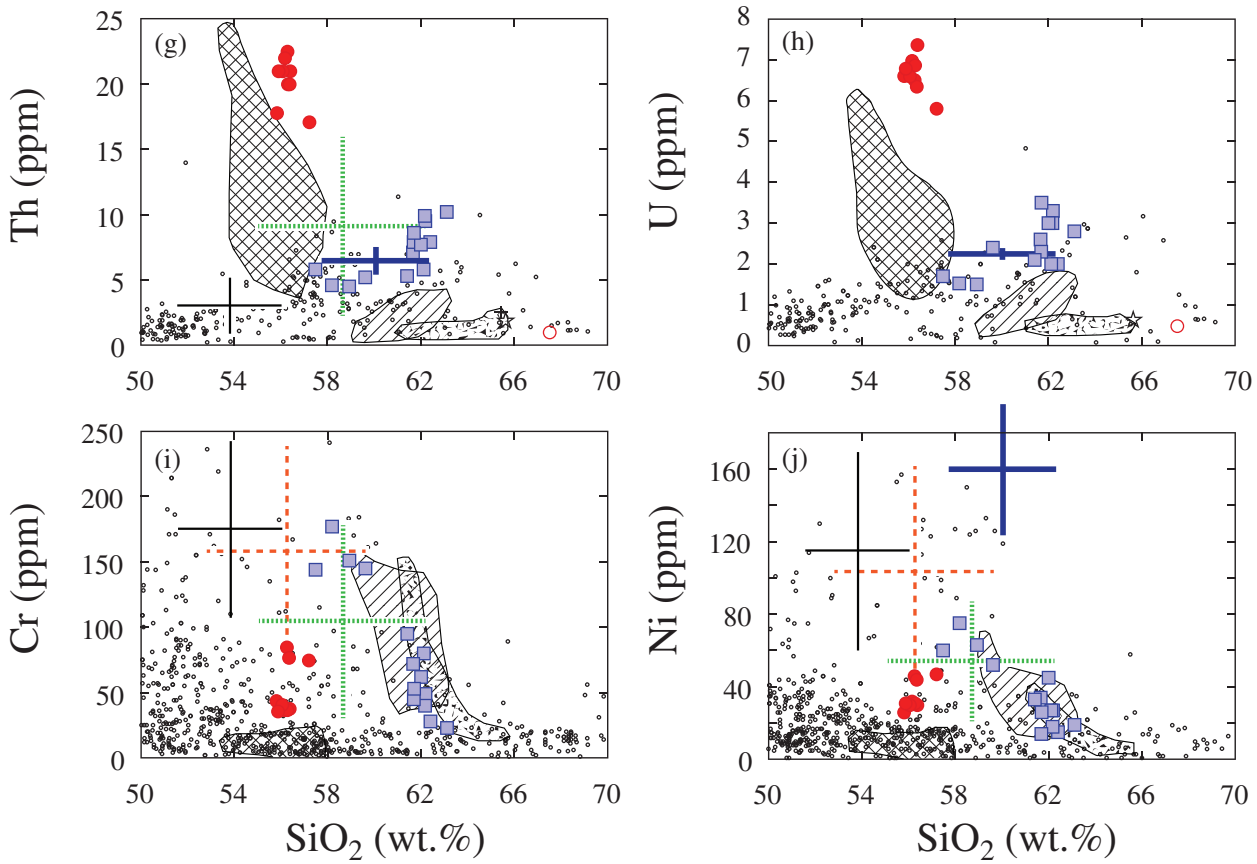

Fig. 7. Continued.

Interstitial melts and melt inclusions

The chemical compositions of interstitial melts and melt inclusions reflect their different textural occurrences (Table 2; Figs 3 and 5; Supplementary Data Table). Melt SiO_2 contents range from 64 to 80 wt %. The lowest SiO_2 contents (64–65 wt %) are those of melt interstitial to clinopyroxene–olivine clusters. Melt inclusions in olivine and clinopyroxene phenocrysts or melts interstitial to clinopyroxene-only or olivine-only clots, as well as melt inclusions in amphibole, have similar SiO_2 contents between 66 and 68 wt %. Melt blebs in the groundmass surrounded by clinopyroxene coronas have a wide range of SiO_2 contents between 65 and 80 wt %. Melt surrounded by clinopyroxene coronas around quartz xenocrysts has SiO_2 contents between 71·5 and 76·0 wt %.

All melt compositions form a continuous variation in plots of SiO_2 versus other major elements. Most major elements (Al_2O_3, CaO, Na_2O, K_2O, P_2O_5, MgO, MnO, TiO_2) correlate negatively with SiO_2. Also, most incompatible and compatible trace elements display a negative correlation with SiO_2, with only Rb displaying a positive correlation, but only between 64 and 72 wt % SiO_2.

The REE patterns of the melts (glasses) are similar to those of the whole-rocks (Fig. 14a). In primitive mantle-normalized trace element patterns, melts are also characterized by an overall similar trend to the whole-rocks, including Nb, Ta, P and Ti negative anomalies and Pb positive anomaly, but differ in their higher Cs, Rb, Th, U, K and Pb and lower Sr and P contents (Fig. 14b).

DISCUSSION

The Quaternary Yuyos andesites are geochemically akin to Archean sanukitoids and, to a great extent, also to Phanerozoic enriched HMA (LSA) (Figs 1, 6, 7 and 8). Petrographically, but less so geochemically, they resemble the sanukitoid lavas of the Setouchi volcanic belt (Japan). Archean sanukitoids and Phanerozoic enriched HMA (LSA) are commonly regarded as the products of melting of mantle peridotite metasomatized by slab melts (Kelemen, 1995; Kelemen *et al.*, 2003; Martin *et al.*, 2005) or as slab melts that have incompletely reacted with mantle peridotite (Rapp *et al.*, 1999, 2010).

In contrast to the above petrogenetic models for Archean sanukitoids and enriched HMA (LSA), the

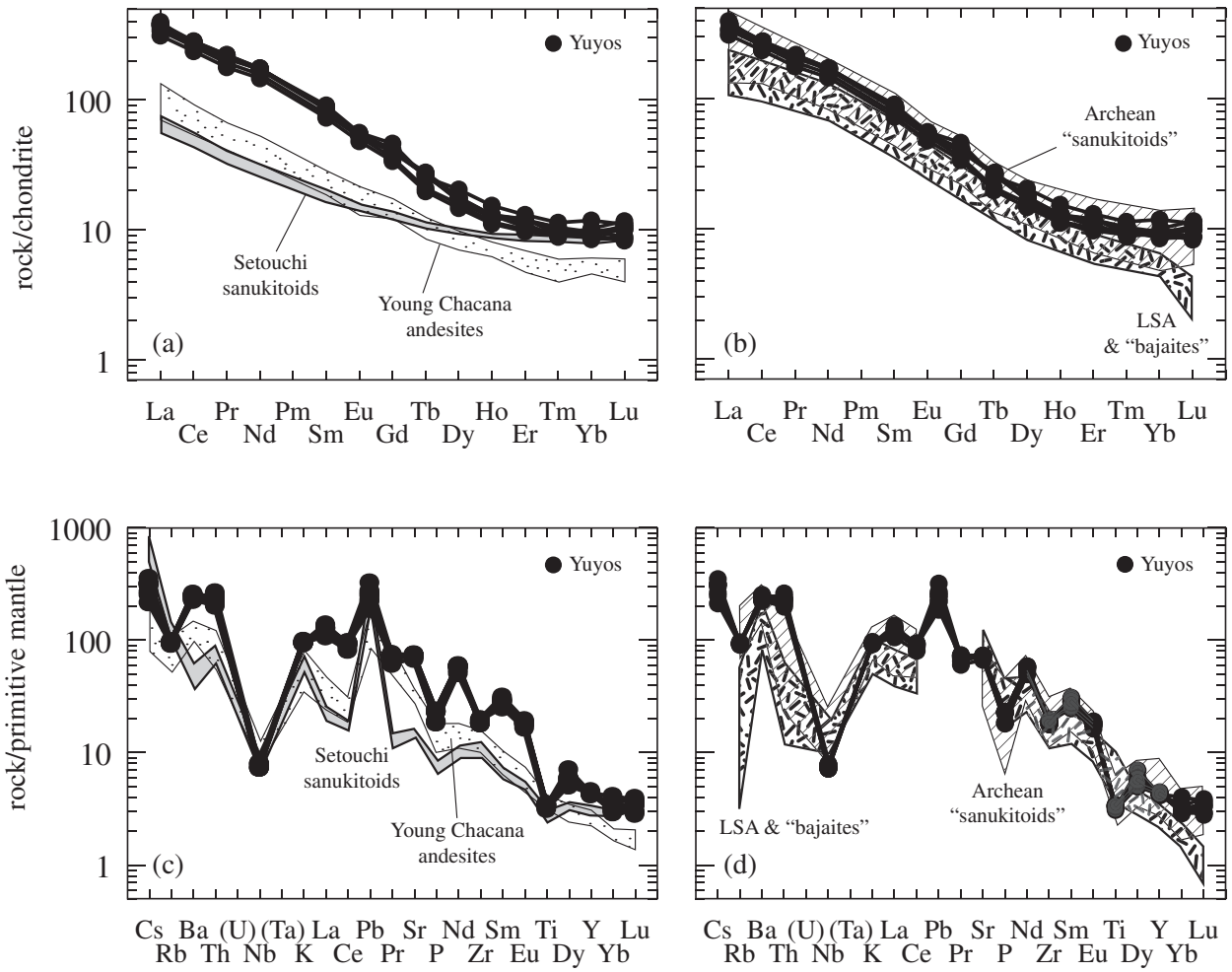

Fig. 8. Chondrite-normalized REE patterns (a, b) and primitive mantle-normalized trace element patterns (c, d) of the Yuyos lava flow compared with 'normal' andesites of Chacana. Also shown are the compositions of low-silica adakites (LSA: Martin *et al.*, 2005), 'bajaites' (Calmus *et al.*, 2003), Archean sanukitoids (Martin *et al.*, 2010), and Setouchi sanukitoids (Shimoda *et al.*, 1998; Tatsumi *et al.*, 2003, 2006). Normalizing values are from Sun & McDonough (1989). Elements within parentheses, although measured for Yuyos rocks (Table 1), are not plotted because they are not available for some of the comparative rocks.

petrographic and geochemical data presented above and discussed below point to an intracrustal origin for the Yuyos sanukitoid-like andesites through magma recharge, mechanical incorporation and partial melting of crystal mushes and/or unconsolidated proto-plutons at different crustal levels (mostly between 0·3 and 0·85 GPa, corresponding to depths between ~10 and ~30 km, based on amphibole geobarometry).

Geochemical arguments for an intracrustal origin of the Yuyos sanukitoid-like andesite

Figure 15 shows the Yuyos andesites and their interstitial melts plotted in various trace element ratio and isotope diagrams together with potential source reservoirs [eclogite slab melt, sediment melt, sediment fluids, mid-ocean ridge basalt (MORB)]. For comparison, the compositions of the 'normal' andesites of Young Chacana, of andesitic to dacitic rocks from three frontal volcanoes of Ecuador (Pilavo, Pichincha, Pululahua) and of high-MgO andesites from the Western Aleutians are also plotted. In all diagrams the Yuyos andesites and their interstitial melts show the strongest affinity with basaltic andesites of the Ecuadorian frontal arc Pilavo volcano. Both Pilavo and Yuyos andesites or glasses are characterized by high Th contents (5–25 ppm; interstitial melts up to 70 ppm), high Th/Nb (1–5) and La/Nb (4–18) ratios, and relatively high Th/La values (0·2–0·4; interstitial melts up to 0·8), which, altogether, distinguish them from the andesitic rocks of other frontal arc volcanoes of Ecuador and normal Young Chacana andesites, as well as from the HMA of the Western Aleutians. High Th, Th/Nb and Th/La values are typically attributed to a sediment-derived melt or

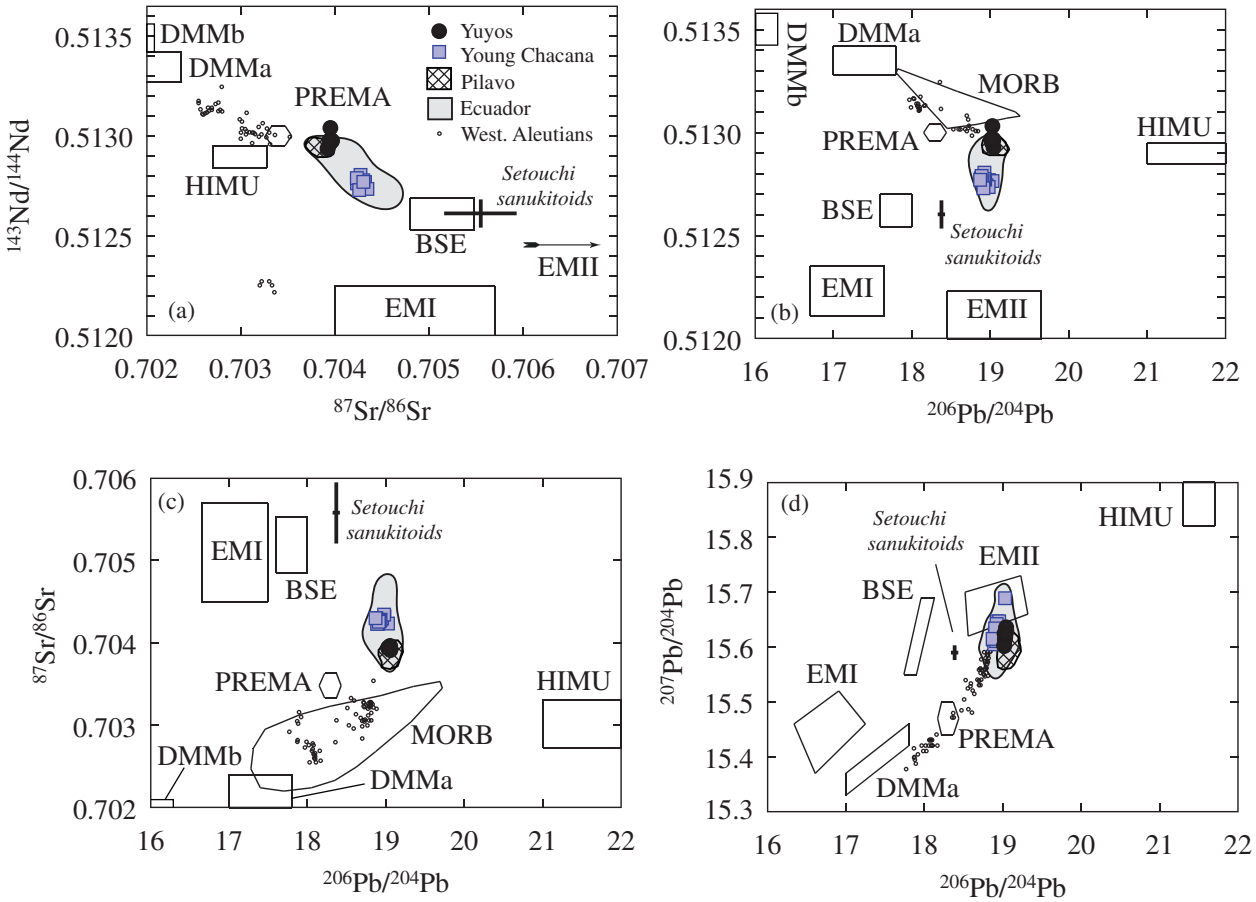

Fig. 9. Sr–Nd–Pb isotope plots of the Yuyos lava flow compared with the 'normal' andesites of Young Chacana, the Pilavo frontal arc volcano, rocks of 12 other volcanic centres in the Northern Andean Zone (data from Bryant *et al.*, 2006; Chiaradia *et al.*, 2009; M. Chiaradia, unpublished data) and HMA of the Western Aleutians (Kelemen *et al.*, 2003). The DMMa (Depleted MORB Mantle a), DMMb (Depleted MORB Mantle b), PREMA (PREvalent Mantle), HIMU (high μ), BSE (Bulk Silicate Earth), EMI (Enriched Mantle I) and EMII (Enriched Mantle II) fields are redrawn from Zindler & Hart (1986).

supercritical fluid component (e.g. Plank, 2005). However, the depleted isotopic compositions of both the Pilavo and Yuyos andesites (the most depleted of the entire Ecuadorian arc and overlapping the most radiogenic compositions of the HMA of the Western Aleutians; Fig. 9) as well as the clear intracrustal nature of the Th-rich, high Th/Nb and Th/La glasses (see below) make this possibility unlikely. From Fig. 15 it is evident that no combination of basaltic or eclogitic slab melt, sediment melt and sediment fluid is able to explain the trace element and isotopic compositions of the Yuyos and Pilavo andesites or glasses. We suggest that intracrustal processes must be responsible for their distinctive geochemical signatures, as also proposed by Plank (2005) for the high Th/La values of arc magmas in general, and by Chiaradia *et al.* (2011) for high Th/La in Pilavo andesites.

Chiaradia *et al.* (2009, 2011) have shown that the andesites of both the frontal and main volcanic arc of Ecuador are largely derived by fractional crystallization accompanied by variable degrees of assimilation and melting of plutonic roots at variably deep crustal levels. Therefore, the distinct trends of the Pilavo and Yuyos andesites with respect to the normal andesites of Chacana and the frontal volcanoes of Ecuador in the Th/Nb vs Th/La, $^{87}Sr/^{86}Sr$ vs Th, and $^{87}Sr/^{86}Sr$ vs La/Nb plots (Fig. 15) seem to suggest fundamental differences in the fractionation and assimilation processes occurring in the petrogenesis of the Yuyos and Pilavo andesites with respect to the other Ecuadorian volcanoes and to 'normal' Young Chacana andesites.

Petrographic and mineral chemistry arguments for an intracrustal origin of the sanukitoid-like andesites of Chacana

In addition to the geochemical arguments presented above, there is compelling petrographic and mineral chemistry evidence for open-system, intracrustal magmatic processes in the genesis of the Yuyos andesites. These processes

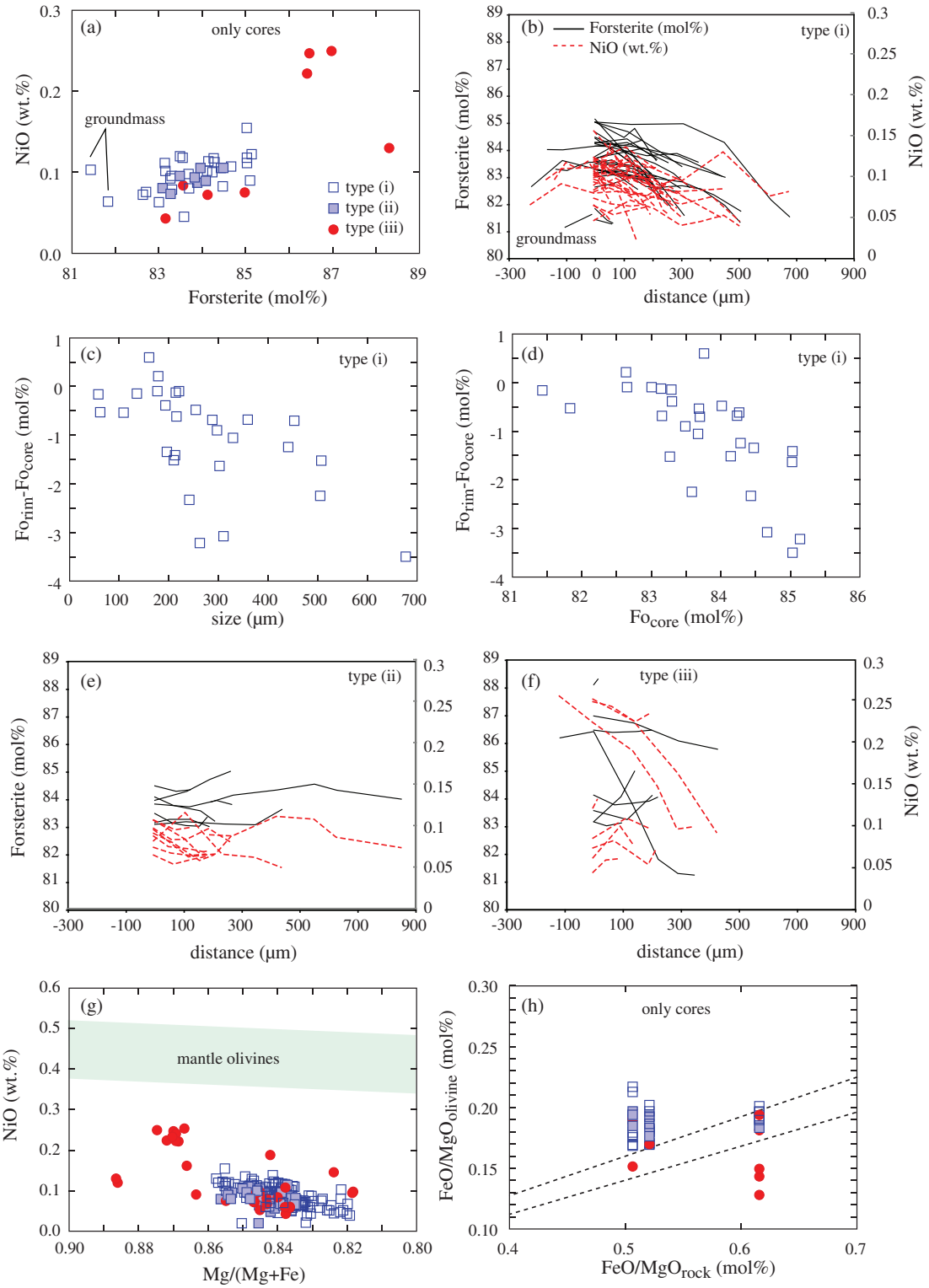

Fig. 10. (a) NiO vs forsterite (mol %) plot of olivines from the Yuyos andesite subdivided into the three types described in Table 2; (b) forsterite (mol %) and NiO (wt %) core-to-rim profiles for type (i) olivines; (c, d) inverse correlations between the difference in forsterite content of cores and rims with olivine crystal size (c) and forsterite core contents (d); (e) forsterite (mol %) and NiO (wt %) core-to-rim profiles for type (ii) olivines; (f) forsterite (mol %) and NiO (wt %) core-to-rim profiles for type (iii) olivines; (g) NiO vs Mg# of olivine, showing that they plot well below the mantle olivine array; (h) FeO/MgO (mol %) of olivine cores vs FeO/MgO (mol %) of the host whole-rock, showing that the great majority of the olivines are xenocrystic because they do not fall within the compositional field (between the dashed lines) of olivines that are in equilibrium with the bulk-rock composition.

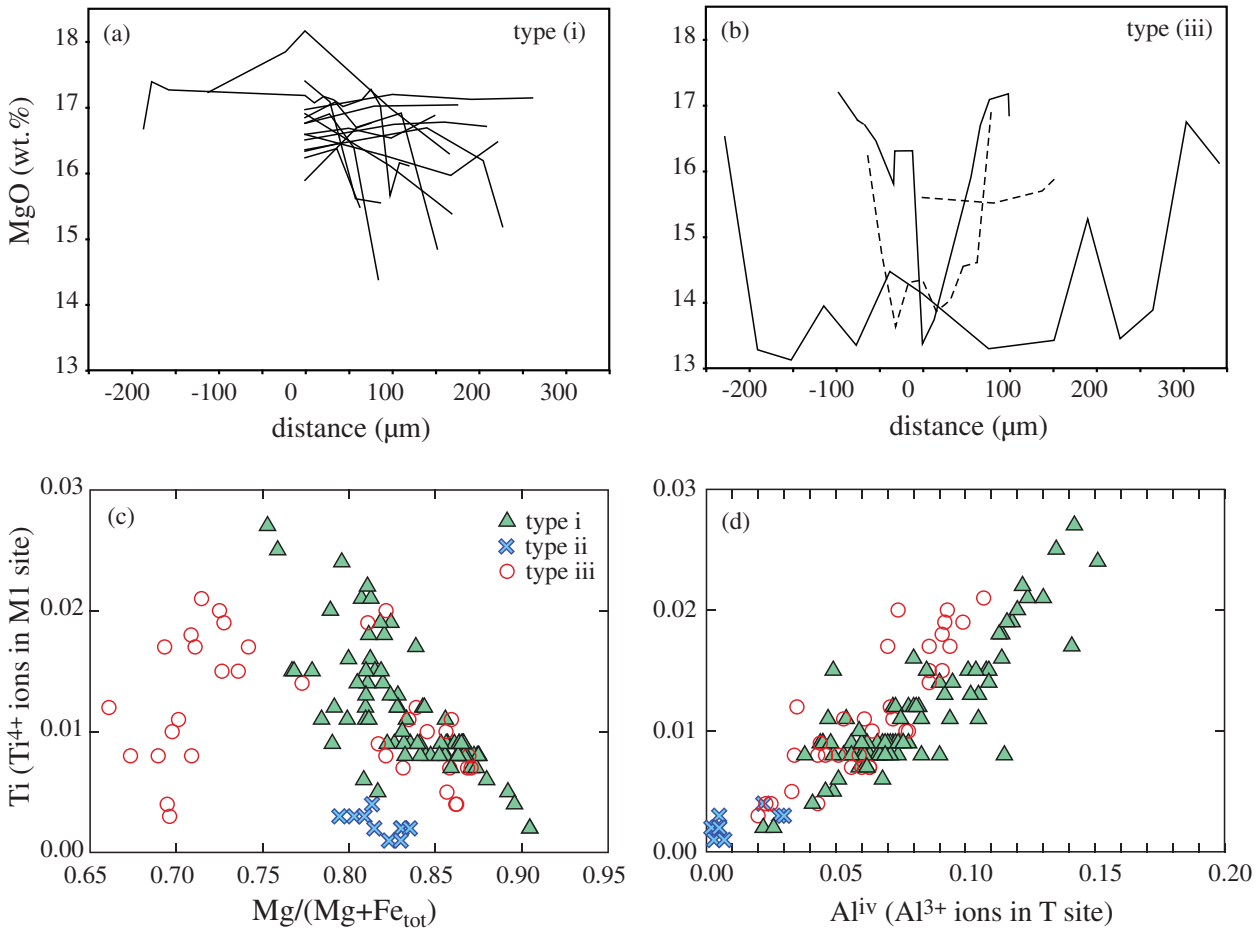

Fig. 11. (a, b) Core-to-rim MgO profiles for type (i) and type (iii) clinopyroxene; (c) Ti vs molar $Mg/(Mg + Fe_{tot})$ and (d) Ti vs Al^{IV} for the clinopyroxenes subdivided into the types discussed in the text.

essentially involve recharge of mafic magma that assimilates and mixes with mafic–ultramafic to intermediate–felsic materials and their partial melt products at various crustal levels.

(1) The occurrence of quartz xenocrysts surrounded by glass (Fig. 4h) or of glass blebs without central quartz, themselves enclosed by a corona of acicular to equant clinopyroxene (Fig. 5e and f), indicates mixing and reaction of quartz-bearing magma, mush or protopluton with a mafic magma. The depleted isotopic signatures of the Yuyos andesites (Fig. 9) make it unlikely that the quartz xenocrysts are derived from highly radiogenic quartz-bearing Paleozoic to Jurassic basement lithologies (Chiaradia *et al.*, 2009). The Mg# of melts in equilibrium with the clinopyroxenes [0·48–0·64; for an $(Fe/Mg)_{cpx}/(Fe/Mg)_{melt} = 0·26–0·30$] crystallized in the coronas around the quartz xenocrysts or glass blebs without central quartz is significantly higher than the Mg# of the glass surrounding the quartz xenocrysts or the glass of the glass blebs without central quartz (0·15–0·28). It roughly corresponds to basaltic andesite or andesite compositions with SiO_2 between 55 and 60 wt % (based on a regression of 145 samples of rocks from 16 Ecuadorian volcanoes) and is also within the Mg# range of the whole-rocks.

(2) The occurrence in the same samples of texturally different olivine phenocrysts (Table 2, Fig. 3a–d) suggests that olivines of different origin were mechanically assembled together. The strongly variable core forsterite contents of all these olivine types, which occur in the same sample at the thin-section scale (Fig. 10b, e and f), support assembly of xenocrystic olivine in equilibrium with variably evolved magmas. Olivine in apparent equilibrium with the host magma displays a systematic core-to-rim decrease of MgO and NiO (Fig. 10b). The difference between core and rim forsterite contents is correlated with the maximum core forsterite contents and with the size of the

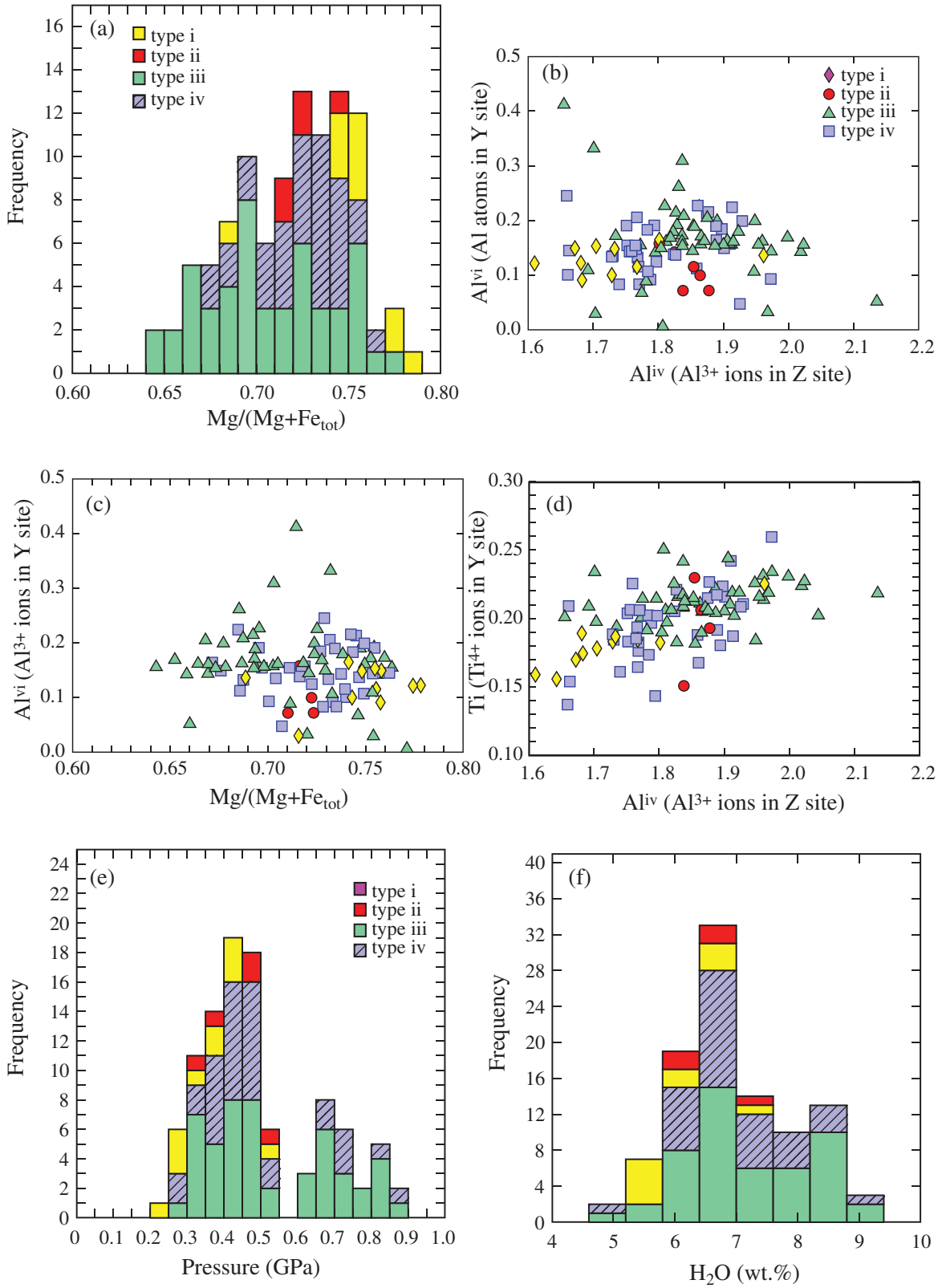

Fig. 12. (a) Mg# [molar Mg/(Mg + Fe$_{tot}$)] histogram for the types of amphiboles discussed in the text; (b) Al^{VI} vs Al^{IV}; (c) Al^{VI} vs Mg/(Mg + Fe$_{tot}$); (d) Ti vs Al^{IV} (see text for discussion). (e) Pressures of amphibole crystallization and (f) H_2O contents of melts in equilibrium with the amphiboles estimated following the methods of Ridolfi *et al.* (2010) and Ridolfi & Renzulli (2012).

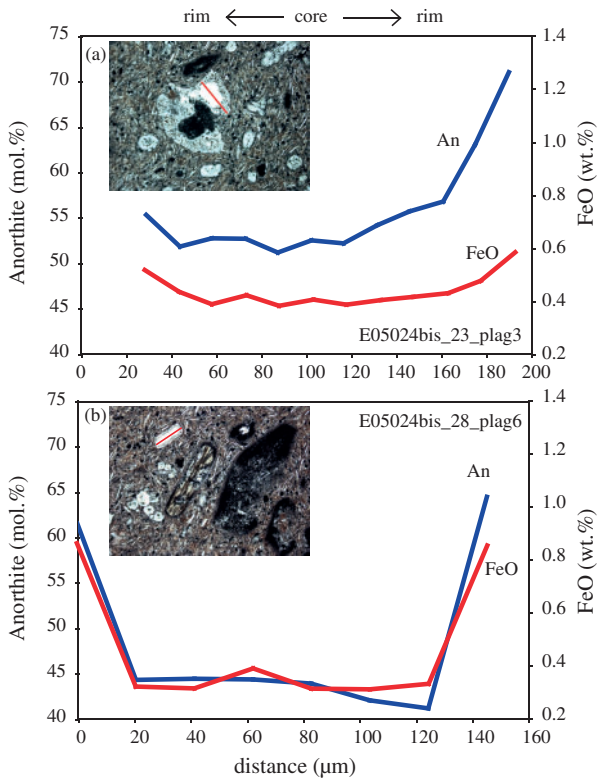

Fig. 13. Core-to-rim profiles of two plagioclase xenocrysts showing reverse anorthite and FeO zoning. The line of the analytical traverse is shown in the photomicrographs.

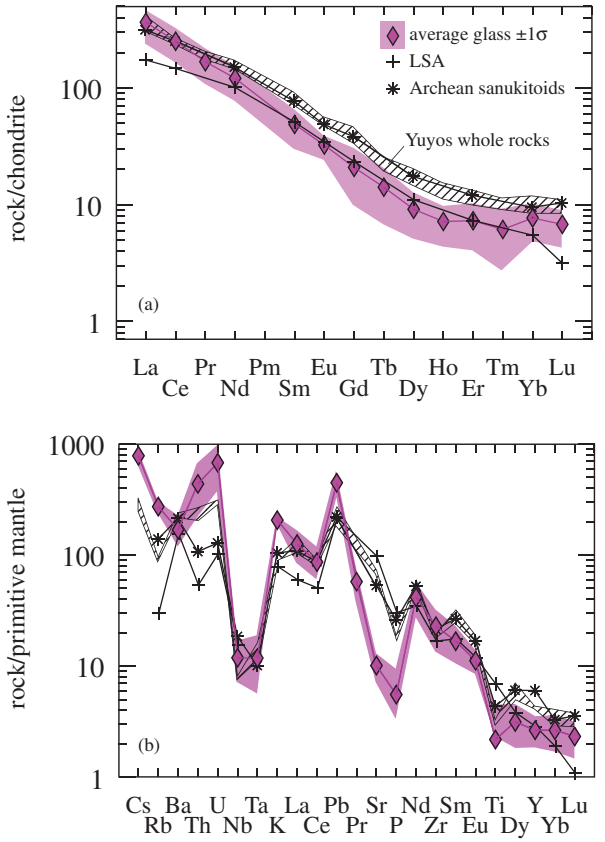

Fig. 14. Chondrite-normalized REE patterns (a) and primitive mantle-normalized trace element patterns (b) of the average composition ±1σ (grey area) of the different glass types ($n = 21$) of the Yuyos lava flow compared with the Yuyos bulk-rock compositions (diagonally hatched area). Also shown are patterns for low-silica adakites (LSA) and sanukitoids from Martin *et al.* (2005, 2010). Normalizing values are from Sun & McDonough (1989).

phenocrysts, the rim forsterite contents being similar at around 82 mol % (Fig. 8c and d). This most probably suggests crystallization of olivines from an evolving magma (with progressively lower MgO) without or with minor Mg diffusion from the Mg-rich core to the Mg-poorer rim (see also Elburg *et al.*, 2006).

(3) Reacted olivine with opacite rims [type (ii)] displays nearly uniform forsterite and NiO contents from core to rim, of 83–85 mol % and 0·05–0·1 wt %, respectively. The cores of most of these olivines, as well as those of fragmented and partly corroded olivines without reaction rims [type (i)], are less forsterite-rich than expected for equilibrium with a magma having the host-rock composition of samples E05022 and E05023 (Fig. 10h). Therefore, both these olivine types are probably cumulitic and their abundant incorporation into the whole-rock has shifted the FeO/MgO of the latter to lower values. This is supported by the higher modal abundance of olivine in samples E05022 and E05023 (~7%) compared with sample E05024 (~3%), in which types (i) and (ii) olivines seem to be in chemical equilibrium with the host-rock [although at least type (ii) olivines, surrounded by thick opacite rims, are clearly not equilibrium phenocrysts].

(4) Reacted olivines associated with or surrounded by amphibole [type (iii)] have cores with variable forsterite and NiO contents, which, in some crystals, are much higher than those of types (i) and (ii) (Fig. 10f). Their forsterite and NiO compositional profiles are characterized by flat, inverse and normal zoning (Fig. 10f). Cores of the forsterite-rich olivines are significantly more forsterite-rich than expected for olivine in equilibrium with the host bulk-rock (Fig. 10h). This supports the petrographic evidence for a xenocrystic origin of such olivine. One possibility is that olivine–amphibole glomerocrysts of xenocrystic origin are recycled olivine-hornblendite cumulates. Early crystallization of amphibole immediately after olivine to form such olivine-hornblendites has been reproduced experimentally under high pressure (0·8 GPa) and water-saturated conditions by Grove

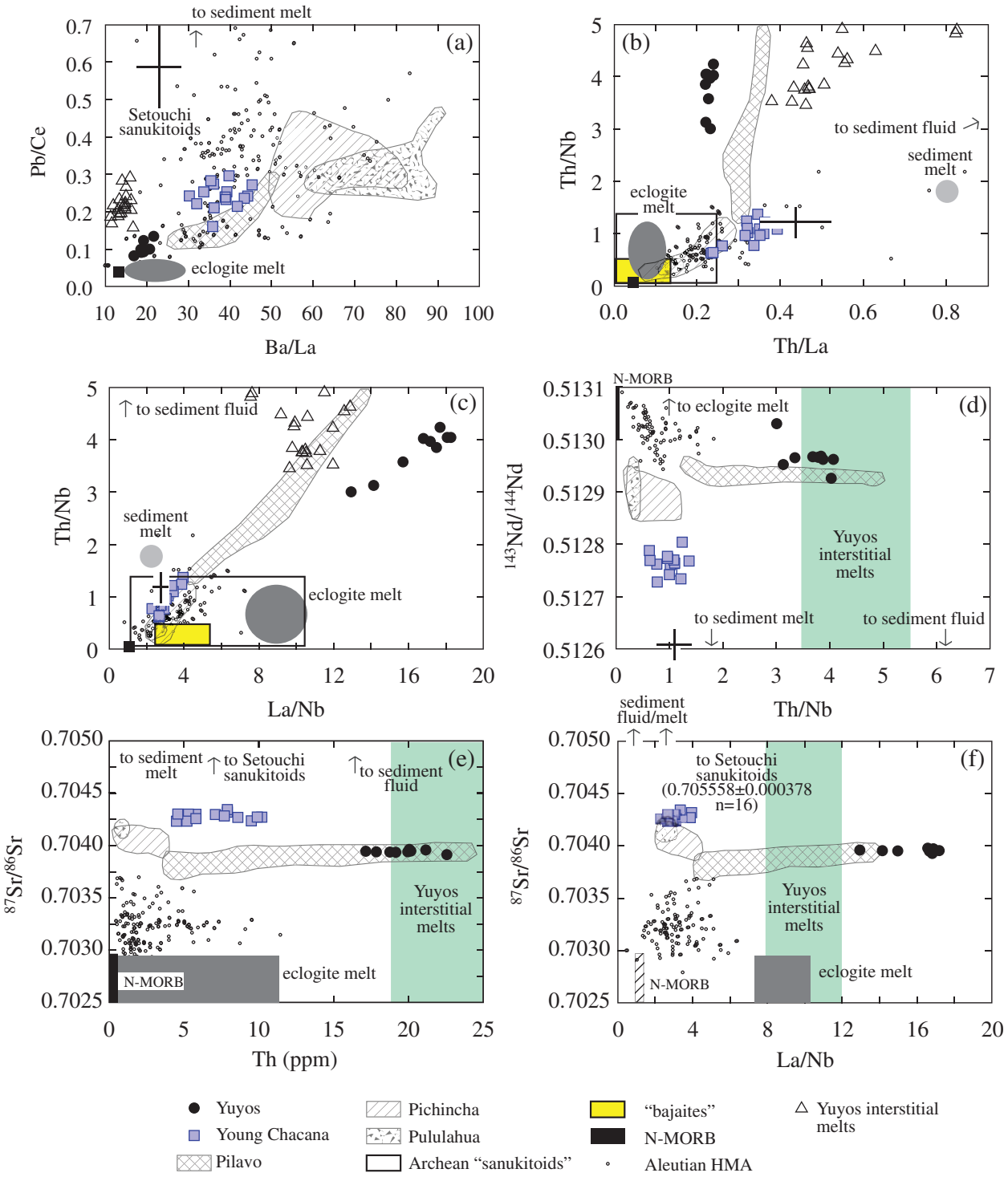

Fig. 15. Trace element ratio plots for Yuyos whole-rocks and interstitial glasses (melts) compared with the 'normal' andesites of Young Chacana, as well as the frontal Pichincha, Pululahua and Pilavo volcanoes. Also shown are the compositions of N-MORB (from GERM database: http://earthref.org/GERM/), sediment melts (Hochstaedter *et al.*, 2001; Kelemen *et al.*, 2003; Chiaradia *et al.*, 2009), sediment fluids (Hochstaedter *et al.*, 2001; Chiaradia *et al.*, 2009), eclogite melt (Rapp *et al.*, 1999; Kelemen *et al.*, 2003), bajaites (Calmus *et al.*, 2003), and sanukitoids (Martin *et al.*, 2010).

et al. (2003) and Krawczynski *et al.* (2012), suggesting that at least part of the differentiation processes of the Yuyos magmas may have occurred at mid- to lower crustal depths. This is consistent with the highest pressures indicated by amphibole geobarometry (Fig. 12e).

(5) Some large clinopyroxene phenocrysts display inverse zoning characterized by a strong MgO (plus Cr and Ni) increase at the outer rims (Fig. 11a), in contact with the groundmass. This suggests a mafic recharge event during which low-MgO clinopyroxene reacted with a more mafic melt with subsequent overgrowth by or re-equilibration with a MgO (Cr, Ni)-richer rim. The clinopyroxene cores are in equilibrium with magmas having Mg# of 0·35–0·4, whereas the rims would be in equilibrium with more mafic magmas having Mg# of 0·55–0·6 [for an $(Fe/Mg)_{cpx}/(Fe/Mg)_{melt} = 0{\cdot}26–0{\cdot}30$]. Based on a compilation of data for Ecuadorian volcanoes to obtain a regression line between SiO_2 and Mg# ($R = 0{\cdot}74$), the clinopyroxene cores would be in equilibrium with a dacitic magma (SiO_2 65–68 wt %), whereas the clinopyroxene rims would be in equilibrium with a basaltic andesite–andesite magma (SiO_2 57–59 wt %).

(6) Inverse anorthite and FeO zoning in plagioclase phenocrysts (Fig. 13) also possibly supports recharge of an evolved magma (cores with $An_{45–60}$) by a more mafic magma (rims with $An_{65–75}$ and higher FeO) or, alternatively, increased pH_2O conditions.

Origin of 'exotic' SiO_2-rich melts

Disequilibrium between 'exotic' melts hosted by, or associated with, olivine and clinopyroxene clots is indicated by the difference between the Mg# of the melts that would be in equilibrium with the olivine (0·61–0·70) and clinopyroxene (0·48–0·64) and the Mg# (0·16–0·38) of the interstitial, 'exotic' melt (glass). The clinopyroxene in the clots armouring glass blebs (Fig. 5b) always forms idiomorphic crystals, which are either acicular or equant. These crystals tend to grow inside the glass globules, sometimes forming single large skeletal crystals with residual vermicular glass inclusions (Fig. 3f), suggesting a peritectic origin of the clinopyroxene (see also Erdmann *et al.*, 2010). Olivine associated with the exotic melts could be residual or peritectic as a result of incongruent melting processes involving interstitial biotite-bearing assemblages (see also Erdmann *et al.*, 2010). We suggest that the exotic melt associated with the olivine ± clinopyroxene clots might be derived from incongruent melting of biotite-bearing intercumulus assemblages within gabbro xenoliths; exotic melts might have formed within a magma chamber by heating owing to hot magma recharge or by decompression during magma ascent. The partially melted and assimilated gabbroic xenoliths that produced the exotic melts must belong to the same magmatic cycle as the recharging magmas and are unlikely to be old fragments (Jurassic to Paleozoic) of the crystalline basement of the Eastern Cordillera, which has more radiogenic Sr isotopic compositions (Chiaradia *et al.*, 2009). In this case, a shift towards more crustal isotopic compositions of Sr and Nd should be observed in the Yuyos andesites, which, in contrast, are the most depleted in Ecuador (Fig. 9).

In addition, the modal abundance and large size (up to 1 cm) of the quartz xenocrysts seem to require interaction with a quartz-bearing crystal mush of more evolved composition. As noted above, it is unlikely that the quartz xenocrysts originated from quartz-bearing basement rocks. Interaction with a magma or mush of more evolved composition is also supported by the MgO-poor core composition of the clinopyroxene xenocrysts and clots (MgO ~13·5 wt % versus 17·5 wt % in cores of 'equilibrium' clinopyroxenes) with inverse zoning, which have crystallized in equilibrium with a dacitic magma (see above), and, possibly, by the anorthite- and Fe-poor composition of the cores of rare plagioclase xenocrysts (see above). We suggest that exotic glass ± quartz surrounded by clinopyroxene coronas derives more probably from *in situ* (i.e. within the magma chamber) or decompression-induced melting of biotite- (± K-feldspar?)-bearing assemblages occurring in fragments of a more felsic crystal mush.

These textural observations are also supported by strong enrichments in K_2O (6–7 wt %), Na_2O (2·5–4·5 wt %) and several incompatible trace elements (Th, U, Pb, Zr, REE, Hf, Ta, Nb) in the interstitial melts, which could derive from partial melting of biotite- (and K-feldspar?)-bearing parageneses (see also Reubi & Blundy, 2008). The occurrence of exotic inclusions in olivine phenocrysts can be explained by partial melting of crystal mushes by mafic recharge at the margins of magma reservoirs (see also Danyushevsky *et al.*, 2004). At least some of the 'exotic' melt might have mingled or mixed with the recharging mafic magma and might have been incorporated in the groundmass where it is no longer identifiable as a distinct component. We note that experimental glasses obtained from dehydration melting of tonalite at intermediate to high pressures (Singh & Johannes, 1996) are K_2O-rich andesitic melts very similar in major element composition to the Yuyos interstitial melts (Fig. 16).

Clinopyroxene–olivine–quartz pseudoternary projection

The bulk compositions of pheno- or xenocryst-poor Yuyos samples are plotted in the clinopyroxene–olivine–quartz pseudoternary projection (projected from plagioclase; Fig. 17) using the projection scheme of Tormey *et al.* (1987) adopted by Sisson & Grove (1993) and Grove *et al.* (2003). For comparison, the plot also shows the bulk compositions of Yuyos and Pilavo amphiboles and interstitial melts, Young Chacana andesites, Pilavo andesites, experimental

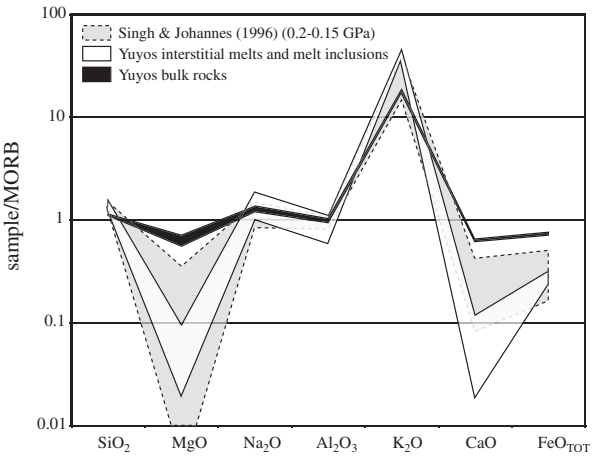

Fig. 16. MORB-normalized major element patterns for the glasses of the Yuyos andesite compared with those of the bulk-rock and experimental glasses derived from partial melting of tonalite at 0·2–1·5 GPa (Singh & Johannes, 1996). MORB normalizing values are from Kelemen *et al.* (2004).

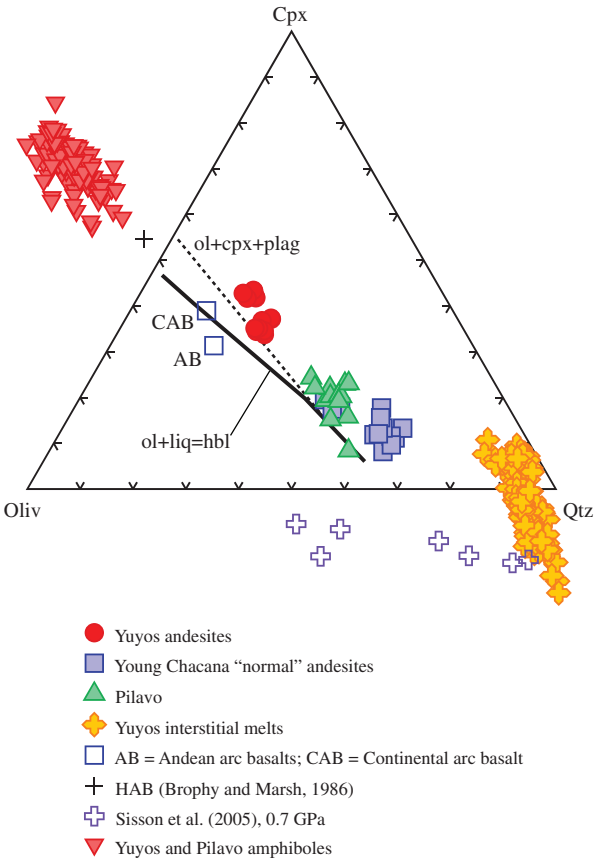

Fig. 17. Clinopyroxene–olivine–quartz pseudoternary plot (projected from plagioclase) for bulk compositions of the Yuyos andesites using the projection scheme of Tormey *et al.* (1987) adopted by Sisson & Grove (1993) and Grove *et al.* (2003). For comparison, also shown are the bulk compositions of Yuyos amphiboles and interstitial melts, normal Chacana andesites, Pilavo rocks, experimental data on partial melting of basalts at 0·7 GPa (Sisson *et al.*, 2005), average Andean arc basalt (AB) and continental arc basalt (CAB) (Kelemen *et al.*, 2004), the olivine + clinopyroxene + plagioclase saturation boundary of basaltic andesite at 0·2 GPa (Grove *et al.*, 2003) and the olivine + liquid = amphibole reaction boundary for hornblende gabbro at 0·2 GPa (Sisson & Grove, 1993). (For discussion see text.)

data for partial melting of basalts at 0·7 GPa (Sisson *et al.*, 2005), the reaction boundary olivine + liquid = hornblende for hornblende gabbro at 0·2 GPa (Sisson & Grove, 1993), and the saturation boundary olivine–clinopyroxene–plagioclase for basaltic andesite at 0·2 GPa (Grove *et al.*, 2003).

Yuyos, Pilavo and Young Chacana andesites are aligned along a trend that passes through the composition of Yuyos and Pilavo amphiboles, suggesting that amphibole fractionation or assimilation has played a role in the evolution of these magmas, as supported by the occurrence of amphibole pheno- or xenocrysts. Interstitial melts in the Yuyos samples overlap in composition with the lowest degree melts of basaltic protoliths at 0·7 GPa (Sisson *et al.*, 2005). Because of the clear crustal origin of these interstitial melts, indicated by petrographic observations (see above), their origin is consistent with high-pressure partial melting of a mafic or intermediate protolith.

Combined with the petrographic evidence discussed above, the clinopyroxene–olivine–quartz pseudoternary projection supports the interpretation that the Yuyos bulk-rock composition can be explained by mixing between olivine–clinopyroxene–amphibole cumulates, intermediate–felsic magmas evolved through amphibole fractionation, partial melts of mafic or intermediate rocks, and recharging mafic magma.

Modelling end-member compositions

The above discussion of geochemical and mineralogical data suggests that the Yuyos sanukitoid-like andesites result from the incorporation of both intermediate–felsic magmas, crystal mushes or protoplutons (e.g. quartz, amphibole, biotite, low-anorthite plagioclase, low-MgO clinopyroxene xenocrysts) and mafic or ultramafic cumulates (olivine xenocrysts) into recharging mafic magmas within the stability field of amphibole–clinopyroxene, but outside that of plagioclase. We can reasonably assume that the Yuyos sanukitoid-like andesite magma contains four major components (Table 3 and Table A1 in Appendix): (i) a bulk intermediate–felsic component evidenced by the occurrence of MgO-poor clinopyroxene xenocrysts, low-anorthite plagioclase xenocrysts, quartz and biotite xenocrysts; (ii) an ultramafic component (olivine–clinopyroxene–amphibole cumulate, perhaps resulting from the fractionation that has produced the intermediate–felsic component above); (iii) an 'exotic' melt component deriving from partial melting of the intermediate–felsic plutonic component (i) above, and of intercumulus mineral phases (biotite, amphibole) in the

Table 3: Compositions used in the calculation of the contributions of the various sources to Yuyos andesites

	SiO_2	TiO_2	Al_2O_3	Fe_2O_{3tot}	MnO	MgO	CaO	Na_2O	K_2O	P_2O_5	Total
Recharging basalt[1]	50·50	0·91	15·50	9·30	0·17	8·40	10·50	3·00	1·10	0·23	99·61
Interstitial melt[2]	66·31	0·77	14·87	2·61	0·06	0·58	1·01	4·07	6·54	0·17	97·02
Assimilated tonalitic pluton or mush (65–68% SiO_2)[3]	64·79	0·52	16·31	4·83	0·07	2·04	4·82	4·10	2·00	0·16	99·64
Average Yuyos composition ($n=9$)[4]	56·43	0·71	15·53	7·08	0·12	5·59	7·49	3·42	2·88	0·41	99·65
Ultramafic component (5%)[5]	39·82	0·01	0·02	15·10	0·32	45·20	0·13	0·01	0·00	0·00	100·61
Recalculated recharging basalt[6]	48·51	0·91	15·50	8·46	0·15	6·14	10·49	3·00	1·10	0·23	94·49
Recalculated recharging basalt normalized to 100%[7]	51·34	0·96	16·40	8·95	0·16	6·50	11·10	3·17	1·16	0·24	100
Continental arc basalt[8]	51·33	0·98	15·70	9·69	0·17	9·48	9·93	2·61	0·88	0·22	100·99
Central American basalt[9]	50·27	1·02	14·60	10·55	0·17	10·63	10·49	2·31	0·77	0·23	101·04
Andean basalt[10]	52·58	1·03	16·66	9·01	0·15	8·28	8·80	2·97	1·19	0·21	100·88
Oceanic arc basalt[11]	50·46	0·91	15·72	9·47	0·17	9·84	11·44	2·35	0·45	0·14	100·95
HAB[12]	49·84	0·92	18·98	10·88	0·19	5·77	10·69	3·36	0·99	0·22	101·84

[1]Calculated as described in Appendix Table A1.
[2]Average of low-SiO_2 (>68 wt %) interstitial melts.
[3]Average of dacitic rocks of Ecuador with SiO_2 between 65 and 68 wt % (in equilibrium with xenocrysts of clinopyroxene in Yuyos andesites).
[4]Average of nine rocks of the Yuyos flow.
[5]Average of olivine compositions in Yuyos andesites.
[6]Composition of the recharging basalt recalculated after subtraction of the ultramafic component.
[7]Composition of the recharging basalt recalculated after subtraction of the ultramafic component and normalization to 100%.
[8]Composition of average continental arc basalt (Kelemen *et al.*, 2004).
[9]Composition of average Central American basalt (Kelemen *et al.*, 2004).
[10]Composition of average Andean basalt (Kelemen *et al.*, 2004).
[11]Composition of average oceanic arc basalt (Kelemen *et al.*, 2004).
[12]Composition of high-alumina basalt (HAB) (Brophy & Marsh, 1986).

ultramafic component (ii), as exotic glasses are found both in association with MgO-poor clinopyroxene and quartz as well as with olivine ± clinopyroxene clots; (iv) the recharging mafic magma.

Here we aim to model the geochemistry and proportion of the recharging mafic magma involved in the petrogenesis of the Yuyos sanukitoid-like andesite magma based on known and assumed compositions (and proportions) of the other components involved in the petrogenetic process (Table 3 and Table A1 in Appendix). Results of these calculations yield a 56 ± 3% contribution from the recharging mafic magma, 23 ± 4% from the exotic glass, 16 ± 5% from the dacitic crystal mush, plus 5% of the ultramafic (dunitic) xenocrystic component. The resulting geochemical composition of the recharging mafic magma is similar to that of average arc basalt, except for the lower MgO and slightly higher CaO and Na_2O, and virtually identical to that of high-alumina basalt (HAB; Fig. 18). Additional calculations carried out considering that the ultramafic component comprised 55% olivine, 40% clinopyroxene and 5% amphibole (i.e. a wehrlite) do not change significantly the final results (Fig. 18). We conclude that the recharging mafic magma could have ranged between continental arc basalt and high-alumina basalt in composition. According to various models (Crawford *et al.*, 1987; Foden & Green, 1992; Müntener *et al.* 2001), high-alumina basalts are produced by high-pressure fractionation of olivine–clinopyroxene (± amphibole) from mantle-derived primitive basalts at the mantle–crust interface or at lower crustal levels. Chiaradia *et al.* (2011) have shown that the basaltic andesites of Pilavo volcano were also derived from mid-crustal evolution of a parental high-alumina basalt.

Petrogenetic model

Mafic to intermediate–felsic plutonic roots are common in volcanic arc systems (e.g. Costa *et al.*, 2002; Dungan & Davidson, 2004; Reubi & Blundy, 2008) but may be hidden by assimilation processes operating both at depth and during magma ascent (e.g. Beard *et al.*, 2005; Erdmann *et al.*, 2010). There is ample petrographic and geochemical evidence that the Yuyos sanukitoid-like andesites contain, within their volumetrically small (<15%) phenocryst population, a significant amount of xenocrystic minerals including olivine, clinopyroxene, amphibole, biotite, plagioclase and quartz.

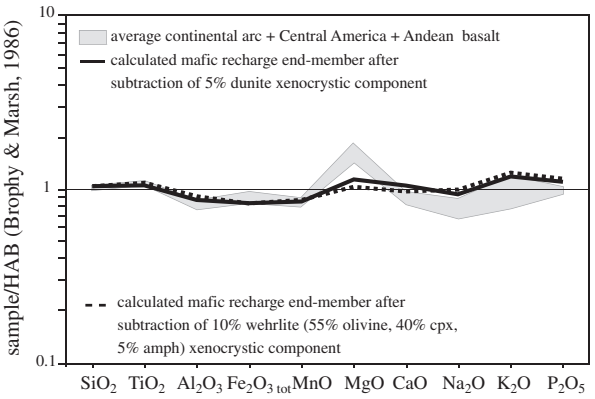

Fig. 18. HAB-normalized major element patterns for the putative recharging mafic magma (after subtraction of 5% dunite or 10% wehrlite, representing the xenocrystic component) compared with those of average continental arc + Central America + Andean basalts. The compositions of continental arc + Central America + Andean basalts are from Kelemen *et al.* (2004). The HAB normalizing values are from Brophy & Marsh (1986).

We suggest that the Yuyos magma resulted from repeated intrusion of mafic magma batches into composite crustal reservoirs occurring at different depths (as suggested by amphibole geobarometry), which caused partial assimilation and melting (probably enhanced during decompression) of quartz-, plagioclase-, biotite- and amphibole-bearing assemblages of intermediate–felsic magma, cumulates, mushes or protoplutons and of intercumulus biotite, amphibole and quartz in their associated mafic–ultramafic cumulates (the plutonic roots of the magmatic system) (Fig. 19). Partial melting resulted in exotic, incompatible element-rich melts, which may have mixed with the incoming mafic magma and have been partly separated from the residual minerals of their protoliths (e.g. Getsinger *et al.*, 2009). The recharging magma was a basaltic arc magma that, before rising to mid-crustal levels, had probably evolved through high-pressure fractionation of olivine–clinopyroxene ± amphibole to become an HAB (see Chiaradia *et al.*, 2011). A process of recharge, fractional crystallization and assimilation like that described above has been shown to be effective in producing relatively undifferentiated magmas that are strongly enriched in incompatible elements (Chiaradia *et al.*, 2009; Lee *et al.*, 2013), like the Yuyos andesites.

Several textural and compositional types of olivine document multiple recharge events. Reacted olivine with opacite rims, as well as forsterite-rich relic olivine associated with or rimmed by opacitized amphibole, might represent one or more early crystallization event(s). Olivine with apparent equilibrium textures might be associated with later mafic recharge, which mixed with forsterite-rich olivine from cumulates and with a more evolved magma, mush or protopluton. The paucity of plagioclase xenocrysts suggests that this mineral never formed and/or was completely assimilated and became unstable under the recharge conditions in the magma reservoir. This is consistent with the high pressure (>10 km depth: Fig. 12e) and high water contents (Fig. 12f) under which the Yuyos magmas evolved. Optically zoned amphiboles, with opacite inner rims separating each zone and with locally inverse MgO zoning, and biotite xenocrysts are further evidence for fractionation and recharge under high pH_2O conditions that favoured the stability of these hydrous minerals. High water contents and high-pressure fractionation in the crust have been proposed for the evolution of Mesoarchean sanukitoid rocks in Brazil (De Oliveira *et al.*, 2010).

The depleted Sr–Nd–Pb isotopic signatures of the sanukitoid-like Yuyos andesite, in contrast to the more radiogenic signatures of the Young Chacana 'normal' andesites, which reflect assimilation of the underlying continental crust basement, indicate that the assimilated rock types belonged to the same magmatic suite as the recharging magma. Such a cannibalistic process implies a relatively long-lived magmatic history, with the formation of crystal mushes that locally insulated subsequent magma recharges from contact with the older continental crust basement. Such a long-lived magmatic plumbing system is consistent with the >2 Myr history of the Chacana caldera (Hall & Mothes, 2008) and might have facilitated the assimilation of its magmatic roots by recharging magmas (see also Grove *et al.*, 2005; Walker *et al.*, 2013).

COMPARISONS OF YUYOS FLOW WITH PHANEROZOIC HMA AND ARCHEAN SANUKITOIDS AND IMPLICATIONS FOR CRUSTAL GROWTH PROCESSES

The Yuyos andesites represent to our knowledge the only sanukitoid-like flow during >2 Myr of magmatic activity in the Chacana caldera complex. Nonetheless, strong geochemical similarities between Yuyos and the Pilavo frontal volcano (Fig. 4) suggest that magmatic processes leading to sanukitoid-like signatures are not isolated cases in the Quaternary volcanic arc of Ecuador. Therefore, a closer inspection of the similarities between the Yuyos andesites and Archean sanukitoids is useful, as well as comparisons with putative Phanerozoic equivalents of Archean sanukitoids.

Archean sanukitoids versus Phanerozoic equivalents (LSA, HMA of Western Aleutians, 'bajaites', Setouchi sanukitoids)

Although the composition of Archean sanukitoids is matched to a good extent by that of Cenozoic and Quaternary enriched high-Mg andesites (HMA; e.g. Kelemen *et al.*, 2003), 'bajaites' (e.g. Calmus *et al.*, 2003), and low-silica adakites (LSA) of Martin *et al.* (2005), there

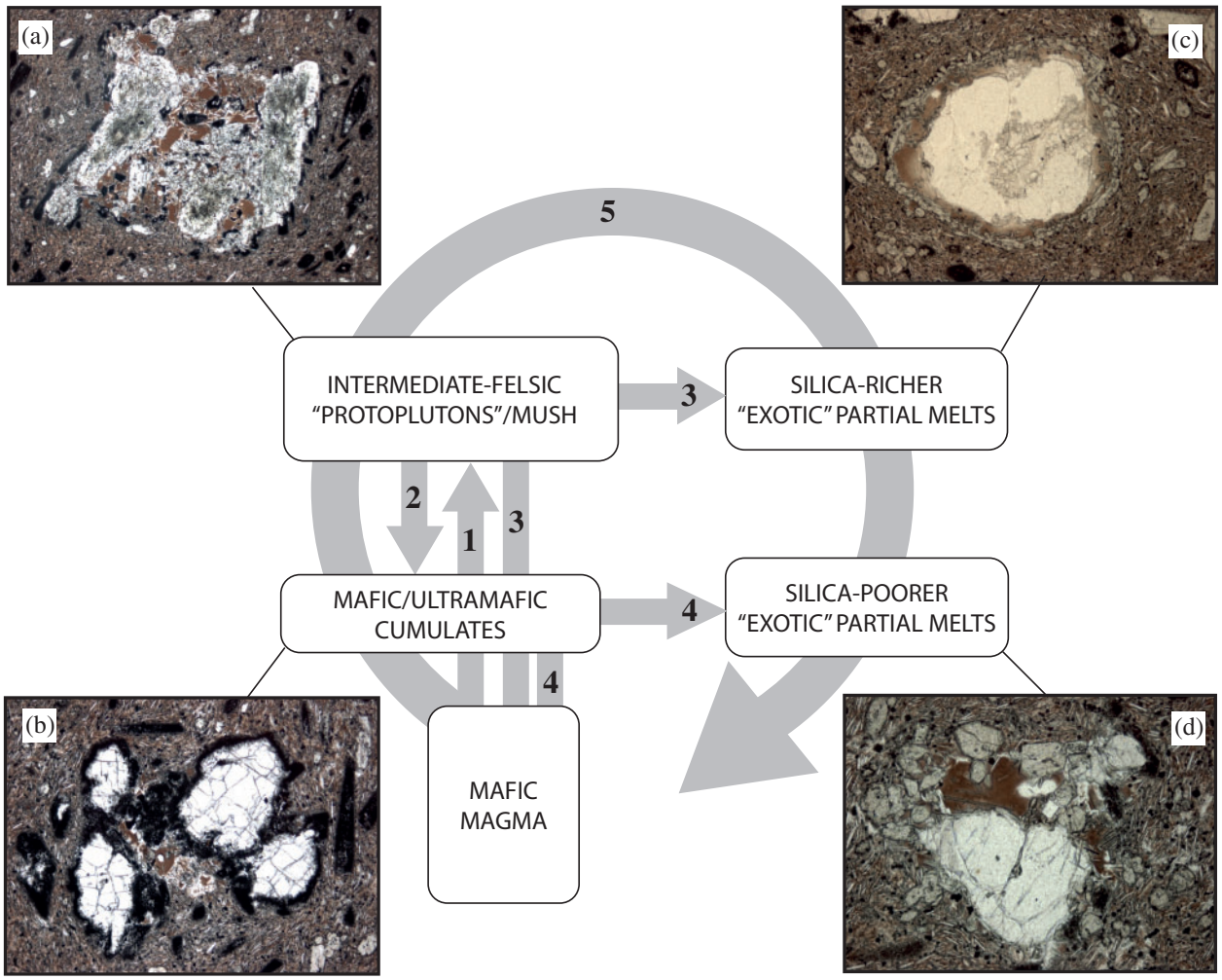

Fig. 19. Schematic model of the petrogenetic processes involved in the formation of the Yuyos sanukitoid-like andesites. Mafic magma rises from the mantle and at different crustal levels evolves to intermediate–felsic 'protoplutons' or mushes (1) [witnessed, among others, by clinopyroxene xenocrysts with inverse zoning; photomicrograph (a)] producing at the same time mafic or ultramafic cumulates (2). Remnants of these mafic cumulates are represented by disequilibrium olivine aggregates [photomicrograph (b)]. A new injection of mafic magma causes partial melting of both the intermediate–felsic 'protoplutons' or mushes (3) [witnessed by the corroded quartz xenocrysts surrounded by melt and a clinopyroxene corona; photomicrograph (c)] and interstitial assemblages of mafic or ultramafic cumulates (4) [photomicrograph (d)]. Further injection of mafic magma blends all the above components (5). Additional partial melting may occur during decompression (see text for more discussion).

are some notable differences (Fig. 1). The Phanerozoic counterparts have somewhat lower Rb, Ba, Th and REE (especially HREE) contents and, except for the Setouchi sanukitoids, a marked positive Sr anomaly compared with Archean sanukitoids (Fig. 1).

Archean sanukitoids differ from LSA and 'bajaites' by having higher REE (especially HREE such as Yb and Lu), Y, Rb and especially Th, but also somewhat lower Cr and Ni (Figs 1, 6 and 7). Also, in the slightly modified trace element pattern of Fig. 1 (in which Sr lies between Ce and Nd) Archean sanukitoids differ from LSA and 'bajaites' in the absence of a positive Sr anomaly and the presence of a strong negative Ti anomaly. Western Aleutian HMA and Setouchi sanukitoids have significantly lower Sr (apart from a few samples), La, Ba, Th, Zr, and U than Archean sanukitoids. Setouchi sanukitoids have also higher Ni contents than Archean sanukitoids.

Chondrite- and primitive mantle-normalized trace element patterns (Figs 1 and 8) show a significant difference between the Setouchi sanukitoids and the Archean sanukitoids, with the former having overall much lower LREE, middle REE (MREE) and other incompatible element contents and a flatter REE pattern. Therefore, in spite of the fact that the name sanukitoid has been applied to Archean high-Mg diorite–tonalite–granodiorite series on the basis of their geochemical similarity to Miocene Japanese volcanic rocks of the Sanuki and Setouchi regions (Shirey & Hanson, 1984), there are marked differences between these two rock types, as also highlighted by Smithies & Champion (2000).

Yuyos andesites versus Archean sanukitoids and Phanerozoic equivalents

In plots of major and trace elements (Figs 6 and 7) as well as in the trace element patterns (Figs 1 and 8) the Yuyos andesites show stronger similarities to Archean sanukitoids than any other potential Phanerozoic equivalent as discussed above. Although Fig. 6 shows that the major element compositions of the Yuyos andesites are most similar to Phanerozoic LSA, in terms of trace elements (Figs 7 and 8) the Yuyos andesites consistently show greater similarity to Archean sanukitoids (particularly evident for La, Yb, Lu, Th, Cr and Ni; Figs 7 and 8), whereas they differ from LSA and 'bajaites' in having significantly higher La and Th and lower Yb. In Sr–Nd–Pb isotope diagrams (Fig. 9), the Yuyos andesites plot at the most evolved end (most radiogenic Pb and Sr and least radiogenic Nd) of the array of MORB-like HMA of the Western Aleutians (Kelemen *et al.*, 2003). In contrast, the Setouchi sanukitoids plot at much more radiogenic Sr and less radiogenic Nd values, in agreement with a strong sediment melt component suggested for their petrogenesis (Tatsumi *et al.*, 2006). In summary, the Yuyos andesites are geochemically very similar to Archean sanukitoids and to a great extent also to Phanerozoic LSA and 'bajaites', whereas both differ markedly from Setouchi sanukitoids. The Yuyos andesites seem to be a closer geochemical proxy for Archean sanukitoids than previously proposed ones, such as LSA and Setouchi sanukitoids.

Although the origin of Archean sanukitoids is beyond the scope of this study, the remarkable similarity of the latter to the Yuyos andesites and their common differences from the putative Phanerozoic equivalents of Archean sanukitoids suggest that intracrustal processes might have also played an important role during the formation of sanukitoid rocks in the Late Archean. The similarity between the adakite- or sanukitoid-like rock association of Ecuador and the TTG–sanukitoid association of the Late Archean further seems to suggest similar geodynamic and magmatic processes in these two environments. As discussed above and by Chiaradia *et al.* (2011), the distinctive 'sanukitoid-like' signatures of Yuyos and Pilavo result from a focused and high rate of magma transit through the crust. Such conditions were realized in the Quaternary arc of Ecuador and are indeed probably similar to those that led to crustal growth episodes during the Late Archean on a more global scale (e.g. Smithies *et al.*, 2009).

CONCLUDING REMARKS

The genesis of Phanerozoic enriched HMA (LSA) is of particular interest for petrologists because these magmatic rocks have geochemical compositions remarkably similar to Late Archean sanukitoids, which represent, together with TTG, the first expression of Earth's felsic continental crust. Their petrogenesis may therefore be critical to understanding the processes responsible for the generation of the continental crust. The common model proposed for the genesis of Phanerozoic enriched HMA (LSA) and Archean sanukitoids involves slab melt–peridotitic mantle interactions occurring in the mantle wedge. However, we have demonstrated that Archean sanukitoids are sufficiently geochemically different from Phanerozoic HMA and other sanukitoid-type rocks that additional (or different?) processes must be involved in their genesis.

Here we have shown that rocks that are geochemically very similar to enriched HMA (LSA) and Archean sanukitoids were formed through intracrustal processes involving the recycling of the mafic–ultramafic to intermediate–felsic plutonic roots of the arc by mantle-derived (possibly high-alumina) basalts. Such a process represents a viable alternative to form enriched HMA (LSA) and sanukitoid-like magmas and should also be considered in models for continental crust generation processes during the Archean.

The geochemistry of the Yuyos sanukitoid-like andesites, situated in the main arc, is similar in many respects to that of basaltic andesites of the frontal arc Pilavo volcano. The across-arc distance between the two volcanic complexes is ~65 km (Fig. 2a). This suggests that geochemical signatures typically attributed to the slab component (e.g. high U, Pb, Th, Th/La and Th/Nb recorded both in the Pilavo and Yuyos andesites) have been refined and enhanced by intracrustal processes in both volcanic edifices; otherwise systematic changes in slab-derived elements should be recorded between the Pilavo and Yuyos andesites, as observed in other frontal versus main arc volcanoes of Ecuador (Barragan *et al.*, 1998; Chiaradia *et al.*, 2009). This highlights the importance of the magmatic plumbing system, in terms of the lifetime and pathways of magmas ascending from the lower crust to the vent, in producing distinctive geochemical features (high Th, Th/La, etc.) at single volcanic edifices. The conditions under which such characteristics are formed are rather uncommon in the Phanerozoic, as shown by the relatively rare association between sanukitoid-like and adakite-like rocks (e.g. in Ecuador), but might have been more common during the Late Archean as shown by the worldwide association of Archean sanukitoids with TTG, probably a consequence of the higher thermal gradient in the Earth at that time (Martin & Moyen, 2002; Keller & Schoene, 2012).

ACKNOWLEDGEMENTS

We thank Marlina Elburg, Kevin Klimm and Bob Stewart for their reviews, which helped to improve the presentation of our work. We are also grateful to Peter Kelemen for sharing his dataset of Aleutian volcanic and plutonic rocks.

FUNDING

This study was funded by the Swiss National Science Foundation (projects N. 200020-126896 and 200020_137663).

SUPPLEMENTARY DATA

Supplementary data for this paper are available at *Journal of Petrology* online.

REFERENCES

Arculus, R. J., Lapierre, H. & Jaillard, E. (1999). Geochemical window into subduction and accretion processes: Raspas metamorphic complex, Ecuador. *Geology* **27**, 547–550.

Aspden, J. A. & Litherland, M. (1992). The geology and Mesozoic collisional history of the Cordillera Real, Ecuador. *Tectonophysics* **20**, 187–204.

Atherton, M. P. & Petford, N. (1993). Generation of sodium rich magmas from newly underplated basaltic crust. *Nature* **362**, 144–146.

Barazangi, M. & Isacks, B. (1976). Spatial distribution of earthquakes and subduction of the Nazca plate beneath South America. *Geology* **4**, 686–692.

Barragan, R., Geist, D., Hall, M., Larsen, P. & Kurz, M. (1998). Subduction controls on the compositions of lavas from the Ecuadorian Andes. *Earth and Planetary Science Letters* **154**, 153–166.

Beard, J. S., Ragland, P. C. & Crawford, M. L. (2005). Reactive bulk assimilation: a model for crust–mantle mixing in silicic magmas. *Geology* **33**, 681–684.

Bourdon, E., Eissen, J. P., Gutscher, M. A., Monzier, M., Hall, M. L. & Cotten, J. (2003). Magmatic response to early aseismic ridge subduction: the Ecuadorian margin case (South America). *Earth and Planetary Science Letters* **205**, 123–138.

Brophy, J. G. & Marsh, B. D. (1986). On the origin of high-alumina arc basalt and the mechanics of melt extraction. *Journal of Petrology* **27**, 763–789.

Bryant, J. A., Yogodzinski, G. M., Hall, M. L., Lewicki, J. L. & Bailey, D. G. (2006). Geochemical constraints on the origin of volcanic rocks from the Andean Northern Volcanic Zone, Ecuador. *Journal of Petrology* **47**, 1147–1175.

Calmus, T., Aguillon-Robles, A., Maury, R. C., Bellon, H., Benoit, M., Cotton, J., Bourgois, J. & Michaud, F. (2003). Spatial and temporal evolution of basalts and magnesian andesites ('bajaites') from Baja California, Mexico: the role of slab melts. *Lithos* **66**, 77–105.

Chiaradia, M. (2009). Adakite-like magmas from fractional crystallization and melting–assimilation of mafic lower crust (Eocene Macuchi arc, Western Cordillera, Ecuador). *Chemical Geology* **265**, 468–487.

Chiaradia, M., Fontboté, L. & Beate, B. (2004). Cenozoic continental arc magmatism and associated mineralization in Ecuador. *Mineralium Deposita* **39**, 204–222.

Chiaradia, M., Müntener, O. & Beate, B. (2011). Enriched basaltic andesites from mid-crustal fractional crystallization, recharge, and assimilation (Pilavo volcano, Western Cordillera of Ecuador). *Journal of Petrology* **52**, 1107–1141.

Chiaradia, M., Müntener, O., Beate, B. & Fontignie, D. (2009). Adakite-like volcanism of Ecuador: lower crust magmatic evolution and recycling. *Contributions to Mineralogy and Petrology* **158**, 563–588.

Corredor, F. (2003). Seismic strain rates and distributed continental deformation in the northern Andes and three-dimensional seismotectonics of the northwestern South America. *Tectonophysics* **372**, 147–166.

Costa, F., Dungan, M. & Singer, B. (2002). Hornblende- and phlogopite-bearing gabbroic crustal xenoliths from Volcán San Pedro (36°S), Chilean Andes: evidence for melt and fluid migration and reactions in subduction-related plutons. *Journal of Petrology* **43**, 219–241.

Crawford, A. J., Falloon, T. J. & Eggins, S. (1987). The origin of island arc high-alumina basalts. *Contributions to Mineralogy and Petrology* **97**, 417–430.

Danyushevsky, L. V., Lelsie, R. A. J., Crawford, A. J. & Durance, P. (2004). Melt inclusions in primitive olivine phenocrysts: the role of localized reaction processes in the origin of anomalous compositions. *Journal of Petrology* **45**, 2531–2553.

Defant, M. J. & Drummond, M. S. (1990). Derivation of some modern arc magmas by melting of young subducted lithosphere. *Nature* **347**, 662–665.

De Oliveira, M., Dall'Agnol, R. & Scaillet, B. (2010). Petrological constraints on crystallization conditions of Mesoarchean sanukitoid rocks, southeastern Amazonian Craton, Brazil. *Journal of Petrology* **51**, 2121–2148.

Dickinson, W. R. (1975). Potash–depth (K–h) relations in continental margin and intra-oceanic magmatic arcs. *Geology* **3**, 53–56.

Dungan, M. & Davidson, J. P. (2004). Partial assimilative recycling of the mafic plutonic roots of arc volcanoes: an example from the Chilean Andes. *Geology* **32**, 773–776.

Ego, F., Sébrier, M., Lavenu, A., Yepes, H. & Egues, A. (1996). Quaternary state of stress in the Northern Andes and the restraining bend model for the Ecuadorian Andes. *Tectonophysics* **259**, 101–116.

Elburg, M. A., Kamenetsky, V. S., Nikogosian, I., Foden, J. & Sobolev, A. V. (2006). Coexisting high- and low-calcium melts identified by mineral and melt inclusion studies of a subduction-influenced syn-collisional magma from South Sulawesi, Indonesia. *Journal of Petrology* **47**, 2433–2462.

Erdmann, S., Scaillet, B. & Kellett, D. A. (2010). Xenocryst assimilation and formation of peritectic crystals during magma contamination: an experimental study. *Journal of Volcanology and Geothermal Research* **198**, 355–367.

Feininger, T. & Seguin, M. K. (1983). Bouguer gravity anomaly field and inferred crustal structure of continental Ecuador. *Geology* **11**, 40–44.

Feininger, T. (1987). Allochthonous terranes in the Andes of Ecuador and northwestern Peru. *Canadian Journal of Earth Sciences* **24**, 266–278.

Foden, J. D. & Green, D. H. (1992). Possible role of amphibole in the origin of andesite: some experimental and natural evidence. *Contributions to Mineralogy and Petrology* **109**, 479–493.

Garrison, J. M. & Davidson, J. P. (2003). Dubious case for slab melting in the Northern volcanic zone of the Andes. *Geology* **31**, 565–568.

Garrison, J. M., Davidson, J., Reid, M. & Turner, S. (2006). Source versus differentiation controls on U-series disequilibria: insights from Cotopaxi Volcano, Ecuador. *Earth and Planetary Science Letters* **244**, 548–565.

Gerstenberger, H. & Haase, G. (1997). A highly effective emitter substance for mass spectrometric Pb isotope ratio determinations. *Chemical Geology* **136**, 309–312.

Getsinger, A., Rushmer, T., Jackson, M. D. & Baker, D. (2009). Generating high Mg-numbers and chemical diversity in tonalite–trondhjemite–granodiorite (TTG) magmas during melting and melt segregation in the continental crust. *Journal of Petrology* **50**, 1935–1954.

Graindorge, D., Calahorrano, A., Charvis, P., Collot, J. Y. & Bethoux, N. (2004). Deep structure of the Ecuador convergent

margin and the Carnegie Ridge, possible consequences on great earthquakes recurrence interval. *Geophysical Research Letters* **31**, doi:10.1029/2003GL018803.

Grove, T. L., Elkins-Tanton, L. T., Parman, S. W., Chatterjee, N., Müntener, O. & Gaetani, G. A. (2003). Fractional crystallization and mantle-melting controls on calc-alkaline differentiation trends. *Contributions to Mineralogy and Petrology* **145**, 515–533.

Grove, T. L., Baker, M. B., Price, R. C., Parman, S. W., Elkins-Tanton, L. T., Chatterjee, N. & Müntener, O. (2005). Magnesian andesite and dacite lavas from Mt. Shasta, northern California: products of fractional crystallization of H_2O-rich mantle melts. *Contributions to Mineralogy and Petrology* **148**, 542–565.

Guillier, B., Chatelain, J. L., Jaillard, E., Yepes, H., Poupinet, G. & Fels, J. F. (2001). Seismological evidence on the geometry of the orogenic system in central–northern Ecuador (South America). *Geophysical Research Letters* **28**, 3749–3752.

Gutscher, M. A., Malavieille, J., Lallemand, S. & Collot, J. Y. (1999). Tectonic segmentation of the North Andean margin: impact of the Carnegie Ridge collision. *Earth and Planetary Science Letters* **168**, 255–270.

Gutscher, M.-A., Maury, R., Eissen, J.-P. & Bourdon, E. (2000). Can slab melting be caused by flat subduction? *Geology* **28**, 535–538.

Hall, M. L. & Mothes, P. A. (2008). The Chacana Caldera Complex in Ecuador. *IOP Conference Series: Earth and Environmental Science* **3**, 012004.

Hochstaedter, A., Gill, J., Peters, R., Broughton, P. & Holden, P. (2001). Across-arc geochemical trends in the Izu–Bonin arc: contributions from the subducting slab. *Geochemistry, Geophysics, Geosystems* **2**, paper no. 2000GC000105.

Jackson, S. E., Longerich, H. P., Dunning, G. R. & Fryer, B. J. (1992). The application of laser ablation microprobe–inductively coupled plasma–mass spectrometry (LAM–ICP–MS) to *in situ* trace element determinations in minerals. *Canadian Mineralogist* **30**, 1049–1064.

Jackson, S. (2008). LAMTRACE data reduction software for LA-ICP-MS. In: Sylvester, P. (ed.) *Laser Ablation ICP-MS in the Earth Sciences: Current Practices and Outstanding Issues. Mineralogical Association of Canada, Short Course Series* **40**, 305–307.

Jaillard, E., Benítez, S. & Mascle, G. H. (1997). Les déformations paléogenes de la zone d'avant-arc sud-équatorienne en relation avec l'évolution géodynamique. *Bulletin de la Société Géologique de France* **168**, 403–412.

Jaillard, E., Soler, P., Carlier, G. & Mourier, T. (1990). Geodynamic evolution of the northern and central Andes during early-to-middle Mesozoic times: a Tethyan model. *Journal of the Geological Society, London* **147**, 1009–1022.

Kay, R. W. (1978). Aleutian magnesian andesites: melts from subducted Pacific ocean crust. *Journal of Volcanology and Geothermal Research* **4**, 117–132.

Kelemen, P. B. (1995). Genesis of high Mg# andesites and the continental crust. *Contributions to Mineralogy and Petrology* **120**, 1–19.

Kelemen, P. B., Hanghoj, K. & Greene, A. R. (2004). One view of the geochemistry of subduction-related magmatic arcs, with an emphasis on primitive andesite and lower crust. In: Holland, H. D. & Turekian, K. K. (eds) *Treatise on Geochemistry*. Elsevier, pp. 593–659.

Kelemen, P. B., Yogodzinski, G. M. & Scholl, D. M. (2003). Along-strike variation in the Aleutian Island Arc: genesis of high Mg# andesite and implications for continental crust. In: Eiler, J. (ed.) *Inside the Subduction Factory. American Geophysical Union, Geophysical Monograph* **138**, 223–276.

Keller, C. B. & Schoene, B. (2012). Statistical geochemistry reveals disruption in secular lithospheric evolution about 2·5 Gyr ago. *Nature* **485**, 490–493.

Kerr, A. C., Aspden, J. A., Tarney, J. & Pilatasig, L. F. (2002). The nature and provenance of accreted oceanic blocks in western Ecuador: geochemical and tectonic constraints. *Journal of the Geological Society, London* **159**, 577–594.

Kilian, R., Hegner, E., Fortier, S. & Satir, M. (1995). Magma evolution within the accretionary mafic basement of Quaternary Chimborazo and associated volcanoes (Western Ecuador). *Revista Geológica de Chile* **22**, 203–208.

Krawczynski, M. J., Grove, T. L. & Behrens, H. (2012). Amphibole stability in primitive arc magmas: effects of temperature, H_2O content, and oxygen fugacity. *Contributions to Mineralogy and Petrology* **164**, 317–339.

Le Bas, M. J., Le Maitre, R. W., Streckeisen, A. & Zanettin, B. (1986). A chemical classification of volcanic rocks based on the total alkali–silica diagram. *Journal of Petrology* **27**, 745–750.

Leake, B. E., Woolley, A. R., Arps, C. E. S. *et al.* (1997). Nomenclature of amphiboles; report of the Subcommittee on Amphiboles of the International Mineralogical Association Commission on New Minerals and Mineral Names. *European Journal of Mineralogy* **9**, 623–651.

Lee, C.-T. A., Lee, T. C. & Wu, C.-T. (2013). Modeling the compositional evolution of recharging, evacuating, and fractionating (REFC) magma chambers: implications for differentiation of arc magmas. *Geochimica et Cosmochimica Acta*, http://dx.doi.org/10.1016/j.gca.2013.08.009.

Litherland, M., Aspden, J. A. & Jemielita, R. A. (1994). *The Metamorphic Belts of Ecuador*. British Geological Survey.

Longerich, H. P., Jackson, S. E. & Günther, D. (1996). Laser ablation–inductively coupled plasma–mass spectrometric transient signal data acquisition and analyte concentration calculation. *Journal of Analytical Atomic Spectrometry* **11**, 899–904.

Lonsdale, P. (1978). Ecuadorian subduction system. *AAPG Bulletin* **62(12)**, 2454–2477.

Mamberti, M., Lapierre, H., Bosch, D., Jaillard, E., Ethien, R., Hernandez, J. & Polvé, M. (2003). Accreted fragments of the Late Cretaceous Caribbean–Colombian Plateau in Ecuador. *Lithos* **66**, 173–199.

Martin, H. & Moyen, J.-F. (2002). Secular changes in tonalite–trondhjemite–granodiorite composition as markers of the progressive cooling of Earth. *Geology* **30**, 319–322.

Martin, H., Moyen, J.-F. & Rapp, R. (2010). The sanukitoid series: magmatism at the Archaean–Proterozoic transition. *Earth and Environmental Science Transactions of the Royal Society of Edinburgh* **100**, 15–33.

Martin, H., Smithies, R. H., Rapp, R., Moyen, J.-F. & Champion, D. (2005). An overview of adakite, tonalite–trondhjemite–granodiorite (TTG), and sanukitoid: relationships and some implications for crustal evolution. *Lithos* **79**, 1–24.

Müntener, O., Kelemen, P. B. & Grove, T. L. (2001). The role of H_2O during crystallization of primitive arc magmas under uppermost mantle conditions and genesis of igneous pyroxenites: an experimental study. *Contributions to Mineralogy and Petrology* **141**, 643–658.

Noble, S. R., Aspden, J. A. & Jemielita, R. A. (1997). Northern Andean crustal evolution: new U–Pb geochronological constraints from Ecuador. *Geological Society of America Bulletin* **109**, 789–798.

Pennington, W. D. (1981). Subduction of the eastern Panama basin and seismotectonics of northwestern South America. *Journal of Geophysical Research* **86(B11)**, 10753–10770.

Pin, C., Briot, D., Bassin, C. & Poitrasson, F. (1994). Concomitant separation of strontium and samarium–neodymium for isotopic analysis in silicate samples, based on specific extraction chromatography. *Analytica Chimica Acta* **298**, 209–217.

Plank, T. (2005). Constraints from thorium/lanthanum on sediment recycling at subduction zones and the evolution of the continents. *Journal of Petrology* **46**, 921–944.

Prévot, R., Chatelain, J.-L., Guillier, B. & Yepes, H. (1996). Tomographie des Andes Equatoriennes: évidence d'une continuité des Andes Centrales. *Comptes Rendus de l'Académie des Sciences, Série II* **323**, 833–840.

Rapp, R. P., Shimizu, N., Norman, M. D. & Applegate, G. S. (1999). Reaction between slab-derived melts and peridotite in the mantle wedge: experimental constraints at 3·8 GPa. *Chemical Geology* **160**, 335–356.

Rapp, R. P., Norman, M. D., Laporte, D., Yaxley, G. M., Martin, H. & Foley, S. F. (2010). Continent formation in the Archean and chemical evolution of the cratonic lithosphere: melt–rock reaction experiments at 3–4 GPa and petrogenesis of Archean Mg-diorites (sanukitoids). *Journal of Petrology* **51**, 1237–1266.

Reubi, O. & Blundy, J. (2008). Assimilation of plutonic roots, formation of high-K 'exotic' melt inclusions and genesis of andesitic magmas at Volcán De Colima, Mexico. *Journal of Petrology* **49**, 2221–2243.

Ridolfi, F. & Renzulli, A. (2012). Calcic amphiboles in calc-alkaline and alkaline magmas: thermobarometric and chemometric empirical equations valid up to 1,130°C and 2·2 GPa. *Contributions to Mineralogy and Petrology* **163**, 877–895.

Ridolfi, F., Renzulli, A. & Puerini, M. (2010). Stability and chemical equilibrium of amphibole in calc-alkaline magmas: an overview, new thermobarometric formulations and application to subduction-related volcanoes. *Contributions to Mineralogy and Petrology* **160**, 45–66.

Roeder, P. L. & Emslie, R. F. (1970). Olivine–liquid equilibrium. *Contributions to Mineralogy and Petrology* **29**, 275–289.

Sage, F., Collot, J.-Y. & Ranero, C. R. (2006). Interplate patchiness and subduction-erosion mechanisms: evidence from depth-migrated seismic images at the central Ecuador convergent margin. *Geology* **34**, 997–1000.

Samaniego, P., Martin, H., Robin, C. & Monzier, M. (2002). Transition from calc-alkalic to adakitic magmatism at Cayambe volcano, Ecuador: insights into slab melts and mantle wedge interactions. *Geology* **30**, 967–970.

Shimoda, G., Tatsumi, Y., Nohda, S., Ishizaka, K. & Jahn, B. M. (1998). Setouchi high-Mg andesites revisited: geochemical evidence for melting of subducting sediments. *Earth and Planetary Science Letters* **160**, 479–492.

Shirey, S. B. & Hanson, G. N. (1984). Mantle-derived Archaean monzodiorites and trachyandesites. *Nature* **310**, 222–224.

Singh, J. & Johannes, W. (1996). Dehydration melting of tonalites. 2. Composition of melts and solids. *Contributions to Mineralogy and Petrology* **125**, 26–44.

Sisson, T. W. & Grove, T. L. (1993). Experimental investigations of the role of H_2O in calc-alkaline differentiation and subduction zone magmatism. *Contributions to Mineralogy and Petrology* **113**, 143–166.

Sisson, T. W., Ratajeski, K., Hankins, W. B. & Glazner, A. F. (2005). Voluminous granitic magmas from common basaltic sources. *Contributions to Mineralogy and Petrology* **148**, 635–661.

Smithies, R. H. & Champion, D. C. (2000). The Archaean high-Mg diorite suite: links to tonalite–trondhjemite–granodiorite magmatism and implications for early Archaean crustal growth. *Journal of Petrology* **41**, 1653–1671.

Smithies, R. H., Champion, D. C. & Van Kranendonk, M. J. (2009). Formation of Paleoarchean continental crust through infracrustal melting of enriched basalt. *Earth and Planetary Science Letters* **281**, 298–306.

Spikings, R. A., Winkler, W., Hughes, R. A. & Handler, R. (2005). Thermochronology of allochthonous terranes in Ecuador: unravelling the accretionary and post-accretionary history of the Northern Andes. *Tectonophysics* **399**, 195–220.

Sun, S. S. & McDonough, W. F. (1989). Chemical and isotopic systematics of oceanic basalts: implications for mantle composition and processes. In: Saunders, A. D. & Norry, M. J. (eds) *Magmatism in the Ocean Basins. Geological Society, London, Special Publications* **42**, 313–346.

Tanaka, T., Togashi, S., Kamioka, H., Amakawa, H., Kagami, H., Hamamoto, T., Yuhara, M., Orihashi, Y., Yoneda, S., Shimizu, H., Kunimaru, T., Takahashi, K., Yanagi, Y., Nakano, T., Fujimaki, H., Shinjo, R., Asahara, Y., Tanimizu, M. & Dragusanu, C. (2000). JNdi-1: a neodymium isotopic reference in consistency with La Jolla neodymium. *Chemical Geology* **168**, 279–281.

Tatsumi, Y. (2006). High-Mg andesites in the Setouchi volcanic belt, southwestern Japan: analogy to Archean magmatism and continental crust formation? *Annual Review of Earth and Planetary Sciences* **34**, 467–499.

Tatsumi, Y. (2008). Making continental crust: the sanukitoid connection. *Chinese Science Bulletin* **53**, 1620–1633.

Tatsumi, Y., Shukuno, H., Sato, K., Shibata, T. & Yoshikawa, M. (2003). The petrology and geochemistry of high-magnesium andesites at the western tip of the Setouchi Volcanic Belt, SW Japan. *Journal of Petrology* **44**, 1561–1578.

Tatsumi, Y., Suzuki, T., Kawabata, H., Sato, K., Miyazaki, T., Chang, Q., Takahashi, T., Tani, K., Shibata, T. & Yoshikawa, M. (2006). The Petrology and Geochemistry of Oto-Zan Composite Lava Flow on Shodo-Shima Island, SW Japan: remelting of a Solidified High-Mg Andesite Magma. *Journal of Petrology* **47**, 595–629.

Todt, W., Cliff, R. A., Hanser, A. & Hofmann, A. W. (1996). Evaluation of a ^{202}Pb–^{205}Pb double spike for high-precision lead isotope analysis. In: Basu, A. & Hart, S. (eds) *Earth Processes: Reading the Isotopic Code. American Geophysical Union, Geophysical Monograph* **95**, 429–437.

Tormey, D. R., Grove, T. L. & Bryan, W. B. (1987). Experimental petrology of normal MORB near the Kane Fracture Zone: 22°–25°N, Mid Atlantic Ridge. *Contributions to Mineralogy and Petrology* **96**, 121–139.

Ulmer, P. (1989). The dependence of the Fe^{2+}–Mg cation-partitioning between olivine and basaltic liquid on pressure, temperature and composition. An experimental study to 30 kbars. *Contributions to Mineralogy and Petrology* **101**, 261–271.

Vallejo, C., Spikings, R. A., Luzieux, L., Winkler, W., Chew, D. & Page, L. (2006). The early interaction between the Caribbean Plateau and the NW South American Plate. *Terra Nova* **18**, 264–269.

Vallejo, C., Winkler, W., Spikings, R. A., Luzieux, L., Heller, F. & Bussy, F. (2009). Mode and timing of terrane accretion in the forearc of the Andes in Ecuador. In: Kay, S. M., Ramos, V. A. & Dickinson, W. R. (eds) *Backbone of the Americas: Shallow Subduction, Plateau Uplift, and Ridge and Terrane Collision* **204**, 197–216.

Walker, B. A., Jr, Klemetti, E. W., Grunder, A. L., Dilles, J. H., Tepley, F. J. & Giles, D. (2013). Crystal reaming during the assembly, maturation, and waning of an eleven-million-year crustal magma cycle: thermobarometry of the Aucanquilcha Volcanic Cluster. *Contributions to Mineralogy and Petrology* **165**, 663–682.

Wood, B. J. & Turner, S. P. (2009). Origin of primitive high-Mg andesite: constraints from natural examples and experiments. *Earth and Planetary Science Letters* **283**, 59–66.

Yaxley, G. M. & Green, D. H. (1998). Reactions between eclogite and peridotite: mantle refertilisation by subduction of oceanic crust. *Schweizerische Mineralogische und Petrographische Mitteilungen* **78**, 243–255.

Yogodzinski, G. M., Kay, R. W., Volynets, O. N., Koloskov, A. V. & Kay, S. M. (1995). Magnesian andesite in the western Aleutian Komandorsky region: implications for slab melting and processes in the mantle wedge. *Geological Society of America Bulletin* **107**, 505–519.

Yogodzinski, G. M., Volynets, M. P., Koloskov, A. V., Seliverstov, N. I. & Matvenkov, V. V. (1994). Magnesian andesites and the subduction component in a strongly calc-alkaline series at Piip volcano, far western Aleutians. *Journal of Petrology* **35**, 163–204.

Zindler, A. & Hart, S. (1986). Chemical geodynamics. *Annual Review of Earth and Planetary Sciences* **14**, 493–571.

APPENDIX

We assume that the Yuyos sanukitoid-like andesite magma contains four major components (Table 3): (i) a bulk intermediate–felsic component (magma, crystal mush, or protopluton), evidenced by the occurrence of MgO-poor clinopyroxene phenocrysts, quartz and biotite xenocrysts; (ii) an ultramafic component (olivine–clinopyroxene–amphibole cumulate), perhaps resulting from fractionation that has produced the intermediate–felsic component above; (iii) an 'exotic' melt component deriving from partial melting of the above two components, as exotic glasses are found both in association with MgO-poor clinopyroxene and quartz, as well as with olivine ± clinopyroxene clots; (iv) the recharging mafic magma. For simplicity we attribute all the olivine phenocrysts (considering all as xenocrystic) to the ultramafic component, although they could partly be attributed to the mafic recharge component. Conversely, we attribute all clinopyroxene and amphibole phenocrysts to the mafic component although they could partly belong to the ultramafic component.

We model the geochemistry and proportion of the recharging mafic magma involved in the petrogenesis of the Chacana sanukitoid-like andesite magma based on known and assumed compositions (and proportions) of the above components involved in the petrogenetic process. For the felsic–intermediate component we assume the composition of an average dacite magma (65 wt % SiO_2) of Ecuador ($n = 35$), which is in equilibrium with cores of the inversely zoned clinopyroxenes. We consider the ultramafic cumulate component as represented by the olivine xenocryst population occurring in the sanukitoid-like andesite magma. We have thus measured the modal abundance of olivine in Chacana sanukitoid-like andesite magma (~5%) by image analysis and have attributed the average composition of all olivine analyses carried out in this study (n ~200) to this end-member. The 'exotic' melt component is represented by the average of 'exotic' melt analyses carried out in this study. Such 'exotic' melt is characterized by intermediate–felsic compositions (64–80 wt % SiO_2) and by incompatible element concentrations systematically higher (K_2O, Na_2O, LREE, Ba, Pb, Th, U, Hf, Ta, Nb, Rb) than, or at least equal (MREE, HREE) to, those of the whole-rocks, and by compatible elements systematically much lower than the whole-rocks. It is therefore a plausible component responsible for the incompatible element enriched signatures of the Yuyos andesite.

Table A1: Contributions from the various components obtained as described in the footnote

Element pair	'Exotic' melt (wt %)	Recharging basalt (wt %)	Assimilated tonalitic pluton or mush (wt %)
Si–Al	20	61	19
Si–Fe	21	61	18
Si–Mg	22	61	17
Si–Ca	20	61	19
Si–Na	23	61	16
Si–K	29	62	10
Al–Fe	20	60	20
Al–Mg	20	60	20
Al–Ca	20	60	20
Al–Na	20	61	19
Al–K	26	49	24
Fe–Mg	21	61	19
Fe–Ca	19	60	22
Fe–Na	22	61	17
Fe–K	29	65	6
Mg–Ca	20	60	20
Mg–Na	22	61	17
Mg–K	29	62	9
Ca–Na	21	61	18
Ca–K	30	67	4
Na–K	28	61	11
Average	23	61	16
1σ	4	3	5

Initially we developed a three end-member mixing model in which exotic melts and the intermediate–felsic end-member have the above constrained compositions and we have calculated the composition of a combined mafic–ultramafic end-member; that is, incorporating both the mafic recharging magma and the olivine xenocryst component (~5% of the whole magma based on image analysis). To do so we have first determined graphically, in plots of SiO_2 versus all major elements, the approximate composition of such a combined mafic–ultramafic component by considering the whole-rock compositions as resulting from mixing of the three end-members above and placing the arbitrary initial condition that SiO_2 content is 50 wt % for the combined mafic–ultramafic component. Such a graphical approach must obey the condition that whole-rock compositions are always enclosed within a triangle having as apices the three end-members above and that the SiO_2 content of the combined mafic–ultramafic end-member is always 50 wt %. After obtaining graphically the approximate major element compositions of the mafic–ultramafic combined end-member for 50 wt %

SiO_2, we have calculated the fractional contributions from each of the three end-members for all possible two major element combinations ($n = 45$) and iteratively readjusted the composition of the combined mafic–ultramafic end-member (including SiO_2) until the standard deviations on the calculated fractional contributions were $\leq 5\%$. By doing so we have obtained a combined mafic–ultramafic end-member composition that is mixed consistently, for all major elements, in the same proportions with the 'exotic' melt and the intermediate–felsic magma end-members to obtain the whole-rock composition (Table 3). Subsequently, we subtract 5% of xenocrystic olivine from the combined mafic–ultramafic component and obtain the composition of the recharging mafic magma. This latter procedure is an oversimplification because olivine phenocrysts may not all be xenocrystic and the ultramafic component might also include clinopyroxene and amphibole xenocrysts (see above). Nonetheless, it provides a first-order approximation of the composition of the recharging mafic magma. Subtracting wehrlite (55% olivine, 40% clinopyroxene, 5% amphibole) instead of dunite does not change the result (Fig. 18).